UiA University of Agder

Master

Exploring high-temperature carbonization effects on petroleum coke for use in sodium-ion battery anodes

TROND ERIK AAGESTAD

SUPERVISORS
Johannes Martin Landesfeind
Børre Tore Børresen

University of Agder, 2024
Faculty of Engineering and Science
Department of Engineering and Sciences

Individual / Group Mandatory Declaration

The individual student or group of students is responsible for the use of legal tools, guidelines for using these and rules on source usage. The statement will make the students aware of their responsibilities and the consequences of cheating. A missing statement does not release students from their responsibility.

1.	I hereby declare that my/our report is my/our own work and that I have not used any other sources or have received any other help than mentioned in the thesis.	Yes
2.	**I further declare that this thesis:** • Has not been used for another exam at another department/university/university college in Norway or abroad. • Does not refer to the work of others without it being stated. • Does not refer to own previous work without it being stated. • Have all the references given in the literature list. • Is not a copy, duplicate or copy of another's work or manuscript.	Yes
3.	I am aware that violation of the above is regarded as cheating and may result in cancellation of exams and exclusion from universities and colleges in Norway, see Universitets- og høgskoleloven §§4-7 og 4-8 og Forskrift om eksamen §§ 31	Yes
4.	I am aware that all submitted theses may be checked for plagiarism.	Yes
5.	I am aware that the University of Agder will deal with all cases where there is suspicion of cheating according to the university's guidelines for dealing with cases of cheating.	Yes
6.	I have incorporated the rules and guidelines in the use of sources and references on the library's web pages.	Yes

Publishing Agreement

Author(s) have copyrights of the thesis. This means, among other things, the exclusive right to make the work available to the general public (Åndsverkloven. §2).
All theses that fulfil the criteria will be registered and published in Brage Aura and on UiA's web pages with author's approval. Theses that are not public or are confidential will not be published.

I hereby give the University of Agder a free right to make the thesis available for electronic publishing:	Yes
Is the thesis confidential? (confidentiality agreement must be completed and signed by the head of the department?	No
Is the task except for public disclosure? (contains confidential information. see Offl. §13/Fvl. §13)	No

Abstract

With the rapid growth of battery usage in both grid-storage and electric vehicle applications, the incentives for exploring alternative batteries outside the traditional lithium-ion batteries have increased exponentially. Sodium, being inherently more abundant with a lower cost, has gained increased interest among researchers in the last decades for its storage capacity and longevity. As the increased atomic radius of sodium present difficulties in using traditional anode materials like graphite, hard carbons have presented desirable properties in recent years following the development of new technology and improved electrode designs. Petroleum coke, a byproduct derived from oil refinery units presents encouraging properties for its use in sodium-battery anodes due to its high-carbon content and porous structure. This thesis aims to present a comprehensive study on the use of petroleum coke as an anode material for SIBs, by first providing a theoretical framework of the working principles that are involved in using heat treated petroleum coke for SIBs, before employing several material and electrochemical analysis techniques to evaluate its performance. Experimental procedures involved treating milled petroleum coke powder at high carbonization temperatures of 950 °C, 1100 °C, 1300 °C, and 1500 °C. These materials was then characterized by employing BET, SEM, XRD, and TGA analyses, before constructing them into half cells and symmetrical cells for battery testing through cycling, CV analysis and EIS. Results indicate that higher carbonization temperatures initially decrease the surface area but reverts to an increase at 1500 °C. The crystallinity was found to increase with temperature, suggesting regional graphitization at 1500 °C. This was further suggested in the visual insights is provided through SEM, where particle size was observed to increase slightly with respect to treatment temperature. The sodium storage capacity measured at 103, 114, 90 and 103 mAh/g for materials treated at 950 °C, 1100 °C, 1300 °C and 1500 °C respectively indicate adequate storage capability for all materials. This was further outlined with an average Coulombic efficiency of 97 % through 50 cycles for the constructed cells. The capacitive nature of the cells was found to be reduced slightly with increasing temperature treatment because of increased reactive sites at the surface. These combined results indicate that while all materials are suitable for use in SIBs, they present differences in material structure that affects the electrochemical performance in different ways. Further analysis is therefore needed to establish the direct implications of these differences when used in energy storage applications.

Contents

Chapter 1

Introduction

1.0.1 Motivation for the thesis

The burgeoning demand for energy storage solutions, along with the rapid growth of the battery sector has sparked significant interest in exploring alternative battery technologies to meet evolving needs. Among these alternatives, sodium-ion batteries (SIBs) have emerged as promising candidates due to their storage capabilities and the abundance of sodium in the Earth's crust, which is approximately a thousand times greater than that of lithium [1], [2]. While initial developments faced challenges related to low energy density compared to their lithium counterparts, recent advancements in materials science and electrode design have reignited the interest in SIBs [3], [4]. The push for sustainable energy solutions, coupled with a growing need for grid-scale energy storage and electric vehicle operation has further fueled the advancements of SIBs, as they may be a very good solution for the challenges in the energy storage industry.

Due to the large ionic-radius of sodium ions (0.102 nm) compared to lithium ions (0.76 nm), graphite and other common carbonaceous anodes that are used for lithium-ion batteries (LIBs) are of limited use in SIBs. This is because of the interlayer-spacing between the graphite layers, which are too small for the sodium to effectively intercalate into the lattice [5], [6]. However, hard carbons have shown great promise due to its porous structure with increased spacing between the carbon layers, providing longevity and great capacity retention through cycling [7], [8]. It has already been established that the achievable capacity from sodium intercalation into hard carbon lies at approximately 300 mAh/g [9]. While higher capacity values have been achieved through doping of heteroatoms, it requires a whole new set of material synthesis procedures that will not be discussed in this thesis [10], [11]. Soft carbon precursors have shown reversible capacities of 100-130 mAh/g with values reaching up to 250 mAh/g with phosphorous doping [12], [13].

With soft carbons in mind, petroleum coke, a byproduct derived from oil refinery units, presents encouraging properties for use in sodium-battery anodes due to its high-carbon content, porous structure and low cost [14]. The material that is extracted contains a high amount of hydrocarbon molecules and sulfuric contents with a rough surface topography, initially rendering the raw material inadequate for anode use [15]. Therefore, thermal treatment is necessary to remove volatiles and optimize the material structure for battery applications. While there have been investigations of the structural changes that occur with increasing temperature in different cokes, the specific impact that higher temperature ranges have on the electrochemical behavior of petroleum coke in SIBs remains underexplored [12], [16]. Investigating this aspect becomes particularly significant as increasing temperatures influence the morphological transformations that occur within the material, directly affecting the electrochemical properties related to sodium intercalation.

1.0.2 Outline of this thesis

To delve into the nuanced relationship that thermal treatment has on petroleum coke for use in SIBs during higher temperatures, this thesis first aims to provide a theoretical framework of the working principles that are involved in using heat treated petroleum coke for SIBs. Through an experimental approach that utilizes various calcination temperatures within the high carbonization range (1000 °C - 1500 °C), and analytical techniques such as thermogravimetric analysis coupled with mass spectrometry (TGA-MS), Brunauer–Emmett–Teller (BET) theory, X-ray diffraction (XRD) analysis, and scanning electron microscopy (SEM), the report then aims to generate a comprehensive material analysis which can be reviewed to assess the effects of high-temperature treatment on petroleum coke. The treated material is then tested in half-cell configurations through charge/discharge cycling. A theoretical approach is used to assess the density and porosity changes of the materials post-treatment. Cyclic voltammetery (CV) analysis will be employed on symmetrical cells constructed with the respective materials. Impedance measurements will also be performed on these cells using electrochemical impedance spectroscopy (EIS). This is done in attempts to evaluate a link between electrochemical performance and the material synthesis that was performed. This work could hopefully yield insights capable of enhancing present-day battery designs and contributing to the development of more efficient SIBs in the future.

Chapter 2

Theory

2.1 The electrochemistry of SIBs and known challenges.

To understand the importance of heat treating carbon materials for SIB application, it is essential to first understand the framework that drives the battery. A commercial SIB contains materials and coordination compounds like sodium cobalt oxide ($NaCoO_2$), sodium nickel oxide ($NaNiO_2$) and prussian blue ($Fe_4[Fe(CN)_6]_3$) as cathode materials [17], [18]. Figure 2.1 illustrates the fundamental working principles of a sodium-ion (Na^+) battery cell with a hard carbon anode, $NaCoO_2$ cathode and sodium hexafluorophosphate ($NaPF_6$) salt as electrolyte.

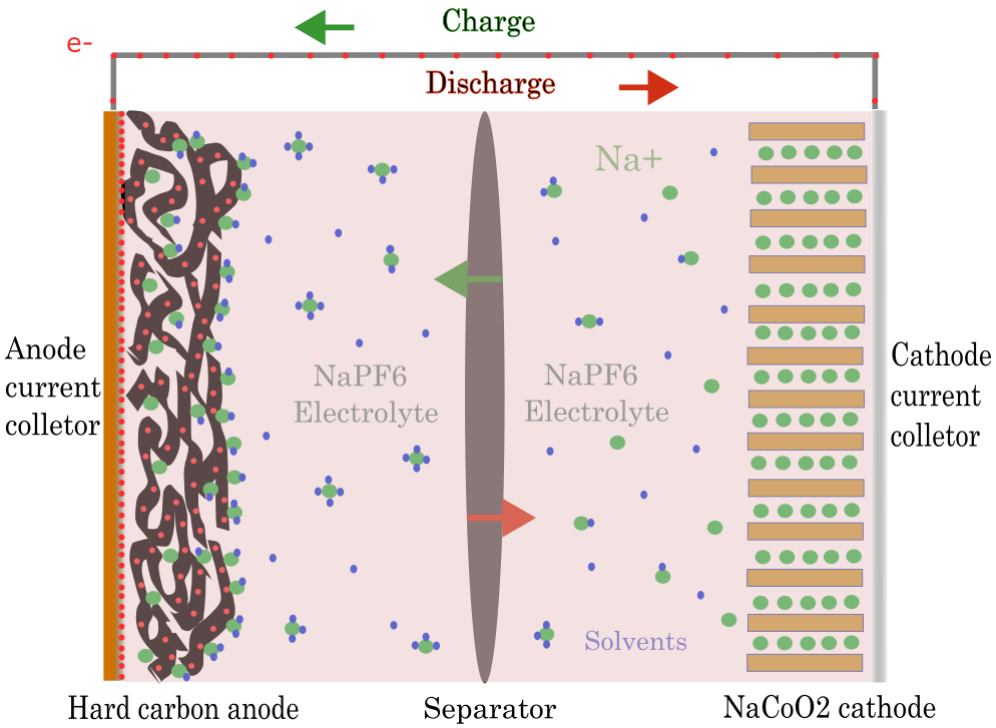

Figure 2.1: A sodium-ion battery illustrating the concept of sodium ions (green dots) moving from the $NaCoO_2$ cathode to the hard carbon anode through solvent molecules (blue dots) in the $NaPF_6$ electrolyte. The current collectors that are isolated due to the separator makes it possible for electrons (red dots) to migrate through the external circuit. The ions and electrons migrate towards the anode during charge and towards the cathode during discharge (Figure created with Inkscape).

To achieve a working electrochemical system capable of reversing sodium insertion, an electrolyte solution containing enough solvents must be present. The electrolyte acts as a medium for ion transport by dissolving the salts and dissociates the ions into cations (posi-

tively charged atoms) and anions (negatively charged atoms). This forms a solution in which the ions can move freely between the two electrodes. The electrodes themselves should be composed of materials capable of facilitating the reversible insertion and extraction of ions between them. In this thesis, the electrodes consist of carbon as the negative electrode and sodium metal as the cathode. The host material typically possess an open structure that allows sodium to intercalate or adsorb within its lattice during charging and discharging cycles. Additionally, a porous separator ensures the function and stability of the battery by prohibiting electron flow, preventing short circuits, while enabling ions to pass through. Lastly, conductive current collectors are necessary to efficiently transfer electrons through the external circuit to the electrodes. For SIBs that use carbonaceous anodes, this ionic transport involves the insertion and extraction of sodium into and from the carbon structure. Half-cell battery configurations are common for explicitly analyzing anode/cathode materials, as only one electrode is acting as the working electrode, allowing for the isolated study of the electrode-electrolyte interface and its intercalative properties. For analyzing the anode properties, a metallic foil composed of the desired working material is used as a counter electrode. This introduces an abundance of ions, refilling whatever ions that may be lost to irreversible side reactions during operation. This leaves the anode material as the only contributor to the changes that are observed during measurements. During charge (sodiation of the anode), the anode undergoes reduction, accepting electrons from the external circuit to intercalate sodium in the carbon structure through a reduction half-cell reaction given by equation 2.1.

$$\mathrm{C} + x\mathrm{Na}^+ + x\mathrm{e}^- \iff \mathrm{NaC}_x, \tag{2.1}$$

where Na^+ represents the sodium ion that intercalates, e^- is the donated electron, and C is the carbon atom in the lattice.

During this process, the cathode undergoes oxidation and donates the electrons. This process is reversed during discharge (desodiation of the anode), releasing the stored energy that was used to form the intercalative bonds. The potential between the anode and cathode is therefore influenced by their respective redox reactions which determines the cell voltage. In a half-cell configuration, referring to the terms charge and discharge can be misleading when in reality, they are attributed to the sodiated and desodiated state of the anode. Therefore, the charge and discharge processes will be referred to as sodiation and desodiation of the anode respectively for the remainder of the thesis.

As an introduction to the theoretical framework provided in this thesis, it is essential to acknowledge the electrochemical challenges encountered in SIBs with carbonaceous anodes. The primary issues arises from the insertion of large sodium atoms into the carbon lattice of graphitic materials, posing difficulties in achieving a capacity range that is comparable to other commercial battery types [19]. This insertion occurs through a wide range of intercalation mechanisms, including adsorption at defect sites, diffusion along and between the interlayer spacing of graphene layers, and adsorption at functional groups on the surface [20]. The interlayer spacing of carbon materials (0.3-0.42 nm) emerges as a key parameter affecting the intercalation process, as the larger ionic radius of sodium requires more space to effectively integrate into the carbon lattice compared to lithium ions [21]. Additionally, the standard reduction potential for $\mathrm{Na}^+ + \mathrm{e}^- \iff \mathrm{Na(s)}$ is -2.71 V versus the standard hydrogen electode (SHE), compared to -3.04 V for the same reaction involving lithium, which influences the rate of ionic transfer through both the electrolyte and electrode [22]. Material properties like porosity and surface topography further dictate the rate of sodium-ion diffusion and the associated reactions [23]. These factors are discussed throughout the report, aimed to provide the reader with the necessary tools to follow the discussion about the effects of high-temperature carbonization on petroleum coke for SIB application.

2.1.1 Sodium intercalation in porous carbon

While graphite is composed of structured graphene layers capable of intercalating lithium between the layers to a high degree, making researchers able to refer to the lithiated state of graphite as LiC_x, this direct analogy cannot be assumed so easily for sodium in porous carbon [24]–[27]. Porous carbon generally possess a disorganized, amorphous structure where the availability of active pores and intercalation sites is influenced by this disordered nature. Therefore, the sodiation mechanism in these types of carbon is more complex, and it is less common to refer to specific states of sodiation as NaC_x. Instead, the increased capacity is attributed to a combination of sodium storage within the disordered structure and adsorption at the surface and within micropores and nanopores. Therefore, the capacity is often described in terms of the specific intercalation mechanisms rather than a specific NaC_x state. Figure 2.2 illustrates a typical sodiation curve and the corresponding intercalation phenomena that occurs within a porous carbon material during decreasing voltage, which better represents the stoichiometry of sodium intercalation in porous carbon.

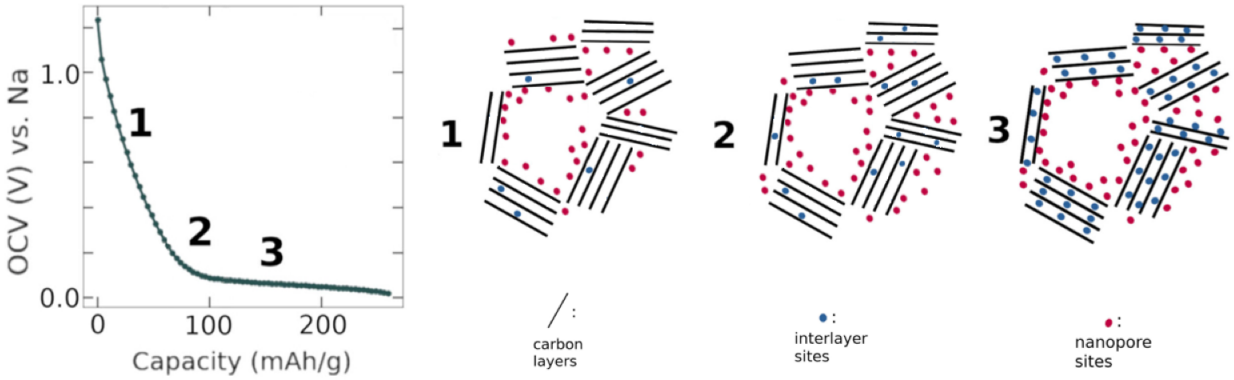

Figure 2.2: The cell voltage profile with respect to capacity explaining the 1) Pore-filling process where available activation sites is occupied by sodium atoms at high voltage ranges. 2) Adsorption of sodium onto nanopore sites and within the pore structure at intermediate voltage ranges. 3) Sodium intercalation stage allocated to insertion between the carbon layers at lower voltage ranges (Figure is adapted with permission from Mercer et al [28]).

During initial sodiation, the majority of Na^+ are adsorbed onto accessible sites within the microstructure, filling the most reactive regions which causes the voltage to drop rapidly. As sodiation progresses, the saturation of the surface sites is reached, causing the intercalation to be favored towards adsorption in nanopores within the material. At the point of reaching low voltage levels, often referred to as plateau voltage (below 0.1V), Na^+ begins to intercalate between the layers of the carbon material alongside any remaining micro or nanoporous sites, contributing to most of the overall capacity of the anode [29], [30]. While a majority of the measured capacity in carbons is assumed to come from the plateau voltage region, distinctions have been observed for materials that have a significant amount of micropores in its structure [29], [31], [32]. It is then reasonable to expect that heat treatment may impact the formation and closing of micropores, which can impact the shape and length of the sodiation curve. This provides to a visual way of comparing the sodiation behavior of different temperature treatments to one another.

As the sodiation process is reversed during desodiation, the curve in figure 2.2 is flipped 180 ° horizontally, increasing the voltage as the ions deintercalate and move back towards the cathode. The total capacity measured from both processes makes it possible to calculate the Coulombic efficiency (CE), often used to describe the reversibility of the intercalation process. The CE can be calculated by using the relation in equation 2.2.

$$\text{CE} = \frac{\text{Desodiation capacity}}{\text{Sodiation capacity}}. \tag{2.2}$$

Since the sodiation process directly attributes to the intercalation properties of the anode material, this equation makes it possible to track the overall efficiency of the reversible processes over prolonged cycling. This measure serves as an indication of the longevity of the battery, and help researchers understand if there is any change in the ongoing electrochemical processes that are occurring over time.

2.2 Structural properties of porous carbon

It is first in the last decades that hard carbons has emerged as an attractive choice for anode materials in SIBs, provided it has undergone some form of heat treatment to make it more suitable for electrochemical applications [33]–[35]. The necessity for such treatment lies in the porous structure that is formed in hard carbons when subjected to high temperatures, enhancing its performance as the interlayer spacing and its internal porosity is optimized, allowing for more effective sodium insertion. Given its mechanical hardness and thermal tolerance, its imperative to understand that the resistance to morphological transformations within the hard carbon material is governed by the chemical bonds that form as carbon atoms become abundant. The well-established octet rule plays a vital role in shaping carbon structures, as the four electrons in the outer shell induce the formation of robust covalent bonds through sp1, sp2 and sp3 hybridization [36]–[39]. This configures the structure in a disorganized manner often described by the "house of cards" model provided by Stevens, et al, resisting further thermal breakdown [9]. It is due to these properties that hard carbons are so inherently resistant to morphological change, and presents the amorphous and porous material structure that is so advantageous for use in SIBs.

2.2.1 Carbonization of petroleum coke

Another aspect that promotes the incentive to thermally treat hard carbon materials is the presence of impurities. Hard carbons often contain hydrogen, heteroatoms and sulfuric components that tend to undergo decomposition or exfoliation from the carbon structure at specific temperatures [40]. When subjected to high enough temperatures, the exfoliation of these remnants leave a porous carbon structure with room for sodium storage. As briefly mentioned before, there are studies indicating the importance of "activated-carbon sites" through doping, outlining that naturally occurring impurities could activate intercalation sites within the structure based on increased interlayer spacing, similar to doping processes [41]–[43]. This becomes significant when talking about carbon materials derived from industries that is rich in heteroatoms, like petroleum coke. Petroleum coke is a soft carbon material that has been modified due to the thermal and cracking treatment during oil refinery processes. Apart from being a low cost material with a high carbon weight %, its internal structure shows promise for use in SIBs as it consists of compact C-C, C-H and C-O-C bonds which grants it the unique property of resisting morphological change at intermediate temperatures. This can cause a porous structure when heated, while also containing a good chunk of heteroatoms for site activation [44]. During the process of carbonization, which occurs at temperature ranges from 1000 - 1500 °C, volatile carbon compounds are

expelled from the coke, causing cracking and rearrangement of the chemical bonds which initially forms a porous structure with an open material surface [45]. Given the reasonable suspicion of increased porosity at elevated temperatures, the density of the materials is expected to change as well. For its use as an anode in SIBs, the electrode porosity $\rho_{electrode}$ can be measured by dividing the electrode weight (g) with the volume of the electrode (cm^3) using equation (2.3).

$$\rho_{\text{electrode}} = \frac{w}{V_t}, \tag{2.3}$$

where w is the weight of the electrode (g) and V_t is the total volume of the electrode (cm^3).

The relationship between electrode density and porosity $P_{\text{electrode}}$ is given by equation (2.4). It provides a way to estimate the porosity of electrodes based on the density of a reference electrode made with untreated petroleum coke.

$$P_{\text{electrode}} = 1 - \frac{\rho_{\text{electrode}}}{\rho_{\text{ref}}}, \tag{2.4}$$

where ρ_{ref} is the measured density of the reference electrode with untreated petroleum coke.

2.2.2 The electrode-electrolyte interface

At the surface of all electrodes, an electrode-electrolyte interface (EEI) is formed. The EEI is a region where various electrochemical processes results in redox reactions and transfer of ions and electrons between the electrode and electrolyte. This interface manifests at the electrode surface, where it interacts with the electrolyte components like ions and solvents [46]. When these ions and solvent molecules come into contact with the electrode surface, they exchange electrons through electrochemical reactions. This phenomenon results in a strong adsorption of ions at the electrode surface, creating a distinct layer known as the double layer [47].

The Stern layer is part of the double layer formed at the electrode surface [48], [49]. It consists of cations and anions from the electrolyte that are attracted to the electrode surface, forming a charge separation layer through electrostatic forces. This layer affects how the ions move near the electrode as a result of the imposed electric field. Together with the diffuse layer, it creates what is known as double layer capacitance, acting like a capacitor at the electrode-electrolyte interface, allowing charge storage within the double layer region.

2.2.3 Solid electrolyte interface formation on carbon anodes

In most electrodes involved in LIBs and SIBs, the EEI extends beyond the double layer to include the formation of a solid electrolyte interphase (SEI) layer [50]. The formation of this passivation layer occurs over the initial charge and discharge cycles, as the electrons at the negative electrode react with the electrolyte components in a redox reaction. This layer is typically composed of various organic and inorganic solvents and salt additives. The layer is of utmost importance, as it acts as a membrane that inhibits electrons from passing but allows for sodium ions to transfer through the film. This prevents further decomposition of the electrolyte and provides protection against electrode degradation. There are extensive literature reviews and quantitative analyses that discuss the impact of electrolyte additives and ionic salts on SEI formation in SIBs [51], [52]. The main parts of discussion outline the importance of choosing the correct electrolyte composition based on the material composition of the battery, as salts and electrolyte solvents react differently across materials.

However, NaPF6 is a commonly used electrolyte salt that serves as a benchmark for most SIBs. It provides good solubility through solvent molecules like ethylene carbonate (EC), ethyl methyl carbonate (EMC), dimethyl carbonate (DMC), and propylene carbonate (PC), while being compatible with carbon materials [53], [54].

When carbons are treated at intermediate temperatures, carbon-compound filaments tend to remain as the volatile components are expelled, introducing an inhomogeneous surface for SEI formation, as can be seen in Figure 2.3.

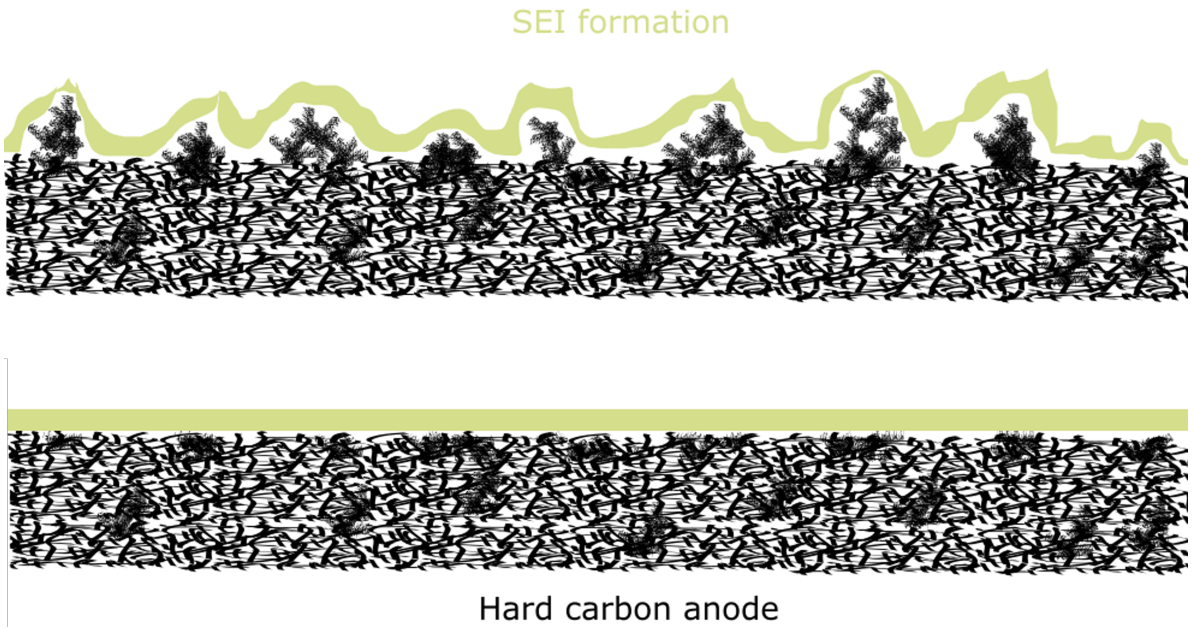

Figure 2.3: The depiction of how an uneven surface topography (top) in hard carbon anodes can influence SEI formation compared to a homogeneous surface (bottom) (Figure created with Inkscape).

Studies done on SEI formation in lithium-ion cells points to structural defects which results in a heterogeneous surface area as a large contributor to a less stable SEI layer [55], [56]. This effect was also found in corresponding studies involving sodium [57], [58]. A comprehensive study done by Hu, et al affirmed through collodial probe microscopy that an inhomogeneous layer forming on the surface could negatively impact the long term cyclic efficiency and stability of SIBs [59].

Moreover, a recent review done by Zhao et al reveal the strong impact of functional groups and heteroatoms at the surface [60]. These groups provide additional nucleation sites for SEI formation to occur, building bridges between the carbon surface and the SEI layer. This promotes stability and reduced impedance at the interface, which are easily overlooked by the incentives to achieve homogeneous SEI formation. Additionally, these functional groups then act as a highway for redox processes to occur as they are easily accessible. This facilitates active sites for sodium adsorption and additional SEI formation over time that could result in increased longevity. Heat treating the carbon materials at higher temperatures will to an extent remove these groups, resulting in a flattened surface with less defects that promotes homogeneous SEI formation [61]. Although a homogeneous area attributes to a more stable SEI formation, it is important to note that the corresponding change in available pore structure on the surface interface are a vital aspect that needs to be considered when optimizing electrochemical performance, as these too might impact SEI formation by presenting additional reactive sites on the carbon surface [62]–[64].

2.2.4 Graphitization degree and interlayer spacing of carbons

Carbonaceous materials are often referred to as graphitizable or non-graphitizable, which relates to what degree of structural ordering can be achieved through temperature treatment. As briefly mentioned, hard carbon have a disorganized structure composed of cross-linked C-C planes and heteroatomic bonds through hybridization. This renders the material resistant to thermal breakdown. Soft carbons do not generally fit the same description, but have a rather organized structure which is prone for further graphitization. While it is common to refer to hard carbons as non-graphitizable, it is important to note that much like soft carbons, hard carbon materials contains composites that can be partially graphitized as the constant realignment of C-C, C-H and C-O-C bonds takes place over the prolonged duration of heat treatment processes [65], [66]. Therefore, the distinct difference between soft and hard carbon materials is the increased resistance to morphological changes, both through mechanical stress and thermal breakdown as a result of their porous structure and cross-linked planes. Due to this, the internal porosity and disorganized cross-planes will remain even at temperatures well over 3000°, resulting in hard carbons being referred to as non-graphitizable [67].

Carbons like petroleum coke will experience a regional breakdown of C-C bonds even during carbonization, causing sites within the structure to be exposed to formation of graphitic domains. This change can to some extent enhance the insertion of sodium ions. The d-spacing may initially increased due to stress graphitization as well as introducing an open pore structure, facilitating ion-insertion between the parallel graphitic domains and available active sites [68]–[70].

A frequent way to determine the interlayer spacing (d-spacing) is through X-ray diffraction. The technique involves beaming a crystalline sample with a given X-ray wavelength (λ) which yields a diffraction angle (θ) based on the crystalline properties of the material, creating a diffraction pattern that can be analyzed to determine the distance between the atomic planes [71]. The relationship between the diffracted beam and the d-spacing is given by Bragg's Law (2.5).

$$n\lambda = 2d \sin\theta, \tag{2.5}$$

where n is the order of interference (normally $n = 1$) and d is the d-spacing given in Angstrom (0.1 nm).

Interlayer spacings are characterized by Miller indicies (d_{hkl}), which describes the orientation of the atomic planes relative to the crystal lattice. For carbon materials, the d002-spacing refers to the distance between the graphitic layers in the hexagonal lattice. Planes indexed as (d100) and (d101) correspond to in-plane atomic arrangements and cross-linked C-C planes, respectively, providing insights into the structure and degree of crystallinity of the material [72]. By analyzing the positions and intensities of the peaks in the XRD pattern, one can get an idea of the structural properties of the material, such as degree of graphitization. This makes XRD a powerful tool for characterizing carbon-based materials and understanding their crystalline properties.

Petroleum coke as a soft carbon can be graphitized to an extent where pores start to collapse, as the constant stress from increasing temperature will break the cross-linked carbon bonds, causing them to realign into more structured configurations. As the d-spacing in the carbon lattice decrease and the active sites are closed off as a result of this change, it becomes increasingly difficult to insert and extract sodium within the structure during battery operation, leading to a point where additional graphitization is unfavorable [73], [74].

A measure for investigating the structural changes within the material is the approximation of the closed pore volume V (cm^3/g), given by equation 2.6.

$$V = \frac{Q \cdot 3.6\mathrm{A}}{\rho \mathrm{F}}, \tag{2.6}$$

where Q is the specific capacity (mAh/g), A is the molar mass of sodium (23g/mol), ρ is the density of sodium metal ($0.97 g/cm^3$) and F is Faraday's constant (96500 C/mol).

This method of calculation is derived from a similar line of work conducted by Biwei Xiao et al, and the incentive emerged in attempts to verify porosity change with increasing temperature [75]. The equation is estimated from the pore-filling model, initially used to provide a rough estimation of capacity based on adsorption and clustering of sodium ions based on Faraday's laws of electrolysis [76], [77]. It is then introduced in the space-filling model from the previous figure 2.2 in section 2.1.1, assuming that Na^+ attach onto the surface of present pores which can be used to estimate the closed pore volume based on capacity [78]. While this equation does prove valuable for estimating the closed pore volume, it contains some uncertainties. Assumptions of ideal behavior and homogeneous pore size may not accurately reflect the real conditions that is occurring. Additionally, the validity of the pore-filling model and potential measurement errors could further contribute to uncertainties in the results.

2.3 Instrumental methods of analysis

2.3.1 Brunauer–Emmett–Teller theory

As previosuly discussed, the surface topography of the anode material used for SIB application is of high importance, as sodium intercalation on active surface sites attribute to a good portion of the total achievable capacity. Therefore, assessing measurements regarding surface properties becomes particularly important for determining the changes that occur during carbonization. A frequent way of measuring the total surface area of a material is through Brunauer–Emmett–Teller theory. The method was constructed by Brunauer, Emmett and Teller in 1938, which utilized gas adsorbent properties at different pressure values to get an overview of the adsorption characteristics of multimolecular layers in the material. This was done by incorporating what is now known as the BET-equation (2.7) [79].

$$\frac{p}{v(p_0) - p)} = \frac{1}{v_m c} + \frac{c-1}{v_m c}(\frac{p}{p_0}), \tag{2.7}$$

where v and v_m is the quantity of adsorbed gas and the monolayer adsorbed gas respectively, p_0 is the saturation pressure of the adsorbate, p is the equilibrium pressure of the adsorbate, c is the BET-constant $= exp(\frac{E_1 - E_L}{RT})$, E_1 is the heat of adsorption for the first layer and E_L is the heat of vaporization.

The equation is derived from the assumption that gas molecules form a monolayer on the surface of the solid material. It relates the quantity of gas adsorbed at a given pressure to the properties of the surface, forming the relation in equation (2.8)

$$S_t = \frac{v_m \mathrm{N} s}{V}, \tag{2.8}$$

where S_t is the total surface area of the sample material (m^2), N is Avogadro's constant ($6.022 \cdot 10^{23}$/mol), s is the cross sectional area of adsorbed molecules and V is the molar volume of adsorbed gas.

By further dividing the total surface area by the mass of the sample, one obtains the specific surface area of the material also known as the BET surface area (BET-SA). It is recognized that the model face limitations when applied to microporous materials due to assumptions regarding monolayer adsorption. Uncertainties surrounding monolayer capacity, surface uniformity, and the influence of micropore filling, could potentially lead to overestimated surface areas, particularly in materials with complex structures like hard carbons [80]–[82]. However, the model remains as one of the most common methodologies to effectively estimate material surface area to date.

2.3.2 Cyclic voltammetry

To further investigate the materials capability of hosting sodium, one can employ a technique known as a cyclic voltammetry (CV) to determine the reduction-oxidation (redox) reactions that occur at a given potential. Figure 2.4 illustrates the concept of CV. By applying a scan rate (mV/s) from an initial voltage (E_1), one can map the current response in a redox-plot from E_1 to the switching voltage (E_2) and the reverse sweep back to E_1.

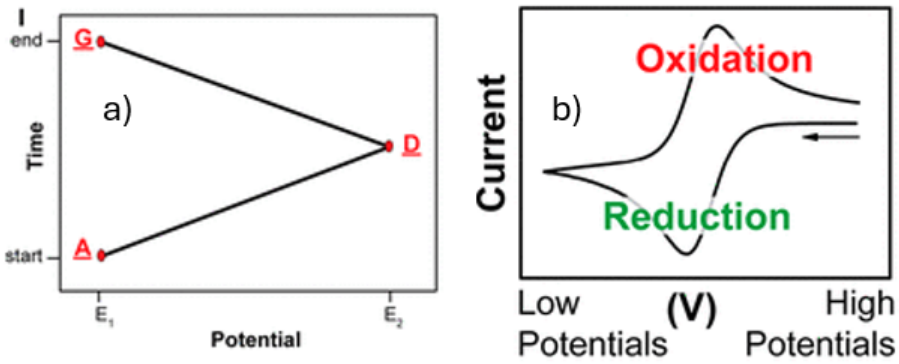

Figure 2.4: a) Shows the voltage sweep curve, where the scan starts at the initial potential E_1 at point (A) before reaching the switching voltage E_2 at point (D) and reversing back to E_1 (G), completing the cyclic voltammetry scan. b) Displays a common redox-reaction plot as a result of the voltage sweep (Figure used with permission from Elgrishi et al [83]).

The method is governed by the ion transport through the electrolyte and diffusion into the electrode. Nernst equation (2.9), which relates the equilibrium potential of an electrochemical cell to the concentration of ions participating in the cell reaction, can be used to observe the system response in cyclic voltammetry by describing how the redox-reactions of electroactive species changes with applied potential.

$$E = E^0 - \frac{\mathrm{R}T}{n\mathrm{F}} \ln \frac{(Ox)}{(Red)}, \tag{2.9}$$

where E and E^0 is the cell potential and the standard cell potential respectively, R is the gas constant (8.314 J/mol·K), T is the temperature in Kelvin (K), n is the electrons transferred in the cell reaction and Ox and Red is the oxidized and reduced analyte components at equilibrium.

The equation is extended from Fick's laws of diffusion and describes how the system response in a CV analysis depends on factors such as the concentration of the electroactive species, the scan rate, and the diffusion coefficient [84], [85]. As the scan rate increases, the diffusion layer becomes thinner as the imposed electric field leads to more rapid transport of the electroactive species, which consequently increases the current response [86], [87]. However, as mentioned in a comprehensive guide for CV analysis provided by Elgrishi, et al, the

electrode-adsorbed species may cause deviations in the observed current response, resulting in an additional term that can be used to describe the observed CV results, given by the modified equation (2.10) [83].

$$i_p = \frac{n^2 \mathrm{F}^2}{4\mathrm{R}T} v A \Gamma, \tag{2.10}$$

where i_p is the redox peak current, v is the scan rate (mV/s), A is the electrode area (cm^2) and Γ is coverage of the adsorbed reactants on the surface (mol/cm^2).

This equation relates the variation in observed current response to the surface-adsorbed species, suggesting that quasi-reversibility or large deviations could be attributed to electron transfer via surface adsorption. Elgrishi et al further mention that if there is no peak-peak separation, which is expected to be present, it could be an indication of adsorbed species at the surface [83]. This is an important notice, as the varying surface topographies encountered in the material synthesis of carbon could directly affect the results observed in this analysis.

2.3.3 Electrochemical impedance spectroscopy

One powerful technique for characterizing the processes occuring at the EEI is electrochemical impedance spectroscopy (EIS). EIS is a non-destructive technique that involves applying a small alternating voltage or current amplitude signal through the cell and measuring the resulting impedance (Z) response across a range of frequencies. The impedance of an electrochemical cell can be given by equation (2.11) [88], [89].

$$Z(\omega) = \frac{\widetilde{V}(\omega)}{\widetilde{I}(\omega)} = |\frac{\widetilde{V}(\omega)}{\widetilde{I}(\omega)}|(\cos\theta(\omega) + \mathrm{j}\sin\theta(\omega)) = Z_r + \mathrm{j}Z_j, \tag{2.11}$$

where $\omega = 2\pi f$ is the angular frequency, θ is the phase angle between the voltage and the current and Z_r and $\mathrm{j}Z_j$ is the real and imaginary part of the resistance respectively where $\mathrm{j} = \sqrt{-1}$.

The imaginary part of the impedance is inversely proportional to the capacitance (C) at a given frequency through the relation

$$Z_{Im} = -\frac{1}{2\pi f C}. \tag{2.12}$$

Given that the capacitance of the cell does not change significantly during the scan, different parts of the battery can be selectively analyzed by varying the frequency range. At high frequencies (MHz-kHz), EIS primarily targets the series resistances, which involve electrode contact resistances with the current collector and the electrolyte [89]. In the mid-frequency range (kHz-Hz), EIS provides information about the properties of the SEI layer. This is because the intermediate frequencies are slow enough to allow for the polarization effects associated with the SEI layer to become apparent but fast enough that the diffusion process does not overshadow this effect [88]. At low frequencies, typically below 1 Hz, EIS investigates the behavior of the EDL at the EEI. These processes involve the slower diffusion of ions through the electrolyte, which is limited by solvent reaction rates, thus requiring low frequencies for accurate analysis[90].

This detailed insight is essential for understanding the electrochemical performance of electrodes. It also serves as a tool to compare the suitability of different electrode materials, as their impedance may vary depending on material composition and structural properties. By analyzing the impedance spectra across these frequency ranges, researchers can optimize

electrode materials for better performance in various applications.

A common way of presenting EIS data is through Nyquist plots, which plots the imaginary part of the impedance (-Im) against the real part of the impedance (Re). The Nyquist plot provide different features such as semicircles and straight lines as shown in figure 2.5, which can be characterized through the frequency ranges discussed previously to achieve an understanding of the introduced impedance from each component in the battery.

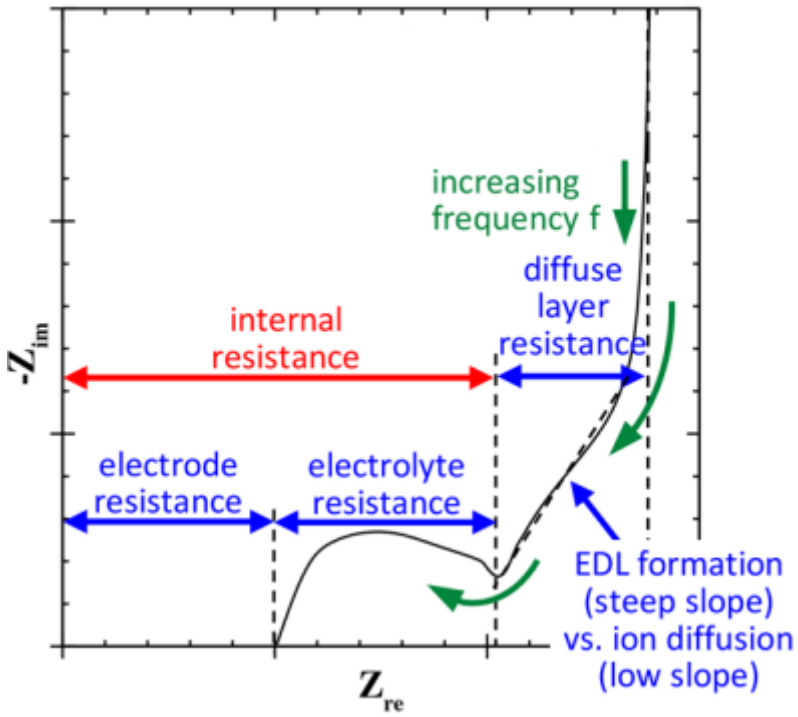

Figure 2.5: The imaginary ($-Z_{im}$) and real (Z_{re}) part of the impedance represented in a Nyquist plot. The semi-circle part of the black curve is attributed to the internal resistances given by the electrode resistance and the electrolyte resistance. The steep 45 ° slope at decreasing frequencies attribute to the diffuse layer resistance and ion diffusion properties, indicating the capacitive behavior of the cell. At very low frequencies, the impedance response is mostly influenced by diffusion, resulting in the vertical line that can be seen at the end of the plot (Figure used with permission from Mei et al [91]).

Chapter 3

Experimental

3.1 Material synthesis

Petroleum coke milling and BET-analysis

The untreated petroleum coke provided by Equinor (Mongstad, Norway) was milled down to a powder by Vianode (Kristiansand, Norway). Vianode also conducted the BET-analysis on the calcined materials to assess the surface area and adsorption characteristics of the materials. Specifics regarding the particle size distribution (PSD) for the materials will be discussed with the BET results in section 4.1.

Material heat treatment

The heat treatment of the material was performed using a PFT-16 Lenton Thermal tube furnace manufactured by Lenton Thermal Designs (now under Carbolite Gero Ltd, Sheffield, UK), with a maximum operating temperature of 1600 °C. In contrast to the industrial approach of rapid heating, a controlled heating and cooling rate of 2 °C/min was employed in an argon atmosphere to thoroughly remove impurities and provide a rigorous treatment process. To gain insight into the carbonization process at various stages, calcination was carried out at temperatures of 950, 1100, 1300, and 1500 °C. The heating process was done by first heating up to a set temperature at 2 °C/min and then a hold time for 1 hour. The cooling process was done by convection at air temperature, where the oven would occasionally produce heat to assure the cooling process did not go below 2 °C/min to avoid thermal shock on the alumina RCA pipe (Carbolite, Sheffield, UK) where the samples were inserted. The treated sample was then extracted before the next sample was inserted and treated at a different temperature in the same way. The selection of these temperatures allowed for comprehensive observation of the pre-carbonization, carbonization, and end-carbonization phases. To avoid confusion, the material samples will be referred to as CC-950, CC-1100, CC-1300 and CC-1500 based on their calcination temperature respectively hereafter.

Thermogravimetric analysis/mass spectrometry setup

The thermogravimetric analysis/mass spectrometry (TGA-MS) was performed by using a TGA/DSC 3^+ apparatus from Mettler Toledo (United States, Colombus, Ohio) connected to a HPR-20 R&D mass spectrometry system from Hiden Analytical (Warrington, UK). The different powders was loaded into small alumina crucibles with a similar weight of approximately ± 30 mg. The software STARe and MASoft10 was used to extract the results from TGA and MS respectively. Initially, the plan was to execute the TGA-MS experiments at 1600 °C under an argon atmosphere to prevent any additional reactions in the material. However, due to glass formation on the sensor from previous experiments, the temperature range was limited to 900 °C to avoid further damaging the instrument. Because of this, an alternative method was employed by heating the material up to 900 °C with a heating rate

of 15 K/min in an oxygen rich atmosphere at 50 ml/min, aiming to create a comparative analysis of its various components through combustion of the material.

Material characterization through SEM and XRD

SEM analysis of the different samples was conducted by Equinor at their research center in Rotvoll (Trondheim, Norway). Imaging of both a powder sample and an electrode sample of the different materials was done at 500x, 1000x and 3000x magnification with an electron high tension (EHT) value of 20 kV and a working distance (WD) of 5.3 - 5.6 mm.

The XRD was performed with a XRDynamic 500 from Anton Paar (Graz, Austria) equipped with a fixed sample stage using petroleum coke powder. A Cu Kα wavelength of 0.154 nm with a scan length of approximately 15 minutes for each material was utilized. The data was collected and made presentable with the XRDview software. It was later discovered that the analysis was conducted by using a divergent beam method, which involves adding a reference standard material like silicon powder to observe the degree of graphitization. This was not done, and the sample was prepared with petroleum coke powder only, introducing no reference standard for peak shifts to be observed. The XRD results will therefore not be able to conclude anything about the change in interlayer spacing and degree of graphitization, but will still be able to shed light on the change in crystalline structure.

3.2 Electrochemical testing

Electrode slurry composition and coating

The slurry was made with a 90:5:5 wt % ratio, composed of 90 % petroleum coke powder, 5 % carbon black (C65 from Gelon Lib, China) and 2.5 % carboxymethyl cellulose (CMC from Gelon Lib, China) in combination with 2.5% styrene butadiene rubber (SBR from Gelon Lib, China) respectively. The mixing procedure for the slurry was initiated using a ARM-310CE Thinky Mixer by firstly thoroughly mixing the dry powders at 500 RPM for 2 minutes before adding the solvents. Deionized water was used as a solvent to prevent the introduction of impurities and was continuously added in small doses between mixing of 2000 RPM for 1 minute until achieving sufficient balance in terms of liquidity and viscosity. The SBR was added at the end and mixed at 500 RPM to avoid thermal decomposition.

The slurry was coated on a copper foil with a TMAX-MS-ZN320B coating machine, applying a 100 μm wet thickness by using an Erichsen D-58675 Model 360 coating bar (Germany) capable of a coating thickness up to 200 μm. The coated foil was dry heated at approximately 80 °C overnight to remove the water contents. The electrodes were punched at a diameter of 16 mm, resulting in an electrode area of approximately 2.01 cm^2. The active material loading of treated petroleum coke for the cells varied between 2.5 mg/cm^2, 2.54 mg/cm^2, 2.3 mg/cm^2 and 1.6 mg/cm^2 for the materials at 950 °C, 1100 °C, 1300 °C and 1500 °C respectively. The electrode thickness was measured at approximately 60 μm for all cells with an error margin of $\pm$ 2 μm (5%) by using a micrometer (293-230-30 series) from Mitutoyo (Japan).

Half-cell construction and testing

Prior to testing, the respective capacity of the cells were calculated by using the theoretical specific capacity of sodium in hard carbon ($\approx$ 300 mAh/g). The capacity was then calculated by multiplying the theoretical capacity with the active material weight measured for each respective cell. Cell construction was conducted and tested at the Institute for Energy Technology (IFE) (Lillestrøm, Norway). The electrodes were heated at 120 °C in an antechamber at vacuum for 8 hours before being transported into a glove box. The construction of the

half cells was done in an argon atmosphere, where the petroleum coke anode, a 25 μm microporous Celgard 2400 membrane (17 mm) with 55 % porosity, 60 μl of 1 M $NaPF_6$ EC:PC (50:50) electrolyte and a piece of sodium foil of 140 μm thickness was attached to a 1.5 mm spacer and compressed with approximately 5 MPa of crimping pressure, with a stack pressure of 1.3 bar. The cells were put on formation cycling within 24 hours at C/20 for three initial cycles between 0.005-1.5 V using a BioLogic BCS-810 tester (BioLogic, France). The cells were then left to cycle at C/10 for a total of 50 cycles. Results were interpreted and made presentable through the coding software Python.

CV analysis and impedance measurements

To perform the CV-analysis, two symmetrical cells of each material were constructed to limit the source of error, using two approximately identical electrodes. In contrast to the half cells, the symmetrical cells were constructed by exchanging the sodium metal foil with a petroleum coke anode, using the anode material as both the working electrode and the counter electrode. Additionally, 50 μl of $LiPF_6$ electrolyte from Gotion (China) with a 3:7 ratio of EC:EMC respectively was added as there was no inventory containing $NaPF_6$. The CV scan was performed in a BioLogic-VMP-3e tester (BioLogic, France) with a scan rate of 10 mV/s, 50 mV/s and 100 mV/s in a cyclic scan from -2 V to 2 V. The impedance measurements was done by applying a sinusoidal amplitude of 10 mV from 200 kHz to 0.1 Hz at -0.2 V - 0.2 V. The results were analyzed and presented through the EC-Lab software from BioLogic.

3.3 Normalized data and uncertainties

Material loading of half cells

A normalization approach was used to better compare the cycling data, as the decline in the mass loading for CC-1300 and CC-1500 was believed to be a result of the elevated temperature treatment that increased material porosity. Consequently, applying a similar solvent content to more porous materials yields a more fluid solution, creating a greater dispersion of particles within the solvent, contributing to reduced mass loading. To better compare the cells based on the same amount of active material, a normalization approach was applied, where the capacity measurements were normalized to the mass of active material in each electrode. This allowed for a more direct comparison of the electrochemical performance of the materials while accounting for the differences in mass loading. The approach makes the assumption that there is a linear relationship between the loading and the observed capacity. This is clearly not the case, as the capacity is affected by several factors like porosity, reactive surface area and impurity content as discussed previously. To support the hypotheses of reduced mass loading due to increased porosity, the average thickness of 10 electrodes was measured from each material, which turned out to be approximately 60 μm for all the electrodes. Further calculations lead to the same results of lower mass loading with respect to elevated temperature, affirming the initial suspicion regarding the porosity. It is therefore important to treat the normalized data with caution, as the capacity is not linearly affected by the amount of active material.

Porosity calculations and assumptions

In attempts to provide additional information regarding the porosity, a theoretical approach was made to estimate the total and open pore volume of the electrode. Given the inverse relationship between density (g/cm^3) and closed pore volume (cm^3/g), the conversion from

density (g/cm^3) to total pore volume (cm^3/g) was done with equation 3.1.

$$\text{Total pore volume of electrode} = \frac{1}{\rho_{\text{electrode}}} = \frac{1}{g/cm^3} = \frac{cm^3}{g} \tag{3.1}$$

This provided a way of estimating the open pore volume by subtracting the closed pore volume from equation 2.6 from the total pore volume. While this introduces additional uncertainties due to the fact that the closed pore volume is derived from several assumptions, it resulted in an additional metric to compare structural changes. It is advised that these calculations are analyzed with this in mind, as the methods may over/underestimate the actual porosity of the electrodes.

Additionally, several electrodes of the untreated petroleum coke was made to obtain the density of the reference electrode needed for equation 2.4. This was done using the same slurry and coating procedure as the other electrodes. The active material weight of the electrodes and their thickness was then measured at average to obtain the density of the reference electrode. This was further used for the porosity calculations presented in the result section. It is important to note that this measures the porosity based on the density of the untreated petroleum coke sample from Equinor as a reference electrode. This density may vary significantly across different types of cokes due to variations in their manufacturing processes.

Internal resistance measurements

A current pulse step corresponding to the C/10 rate was applied to the half-cell batteries for 1 millisecond in between each sodiation and desodiation stage, measuring the system response in attempts to get internal resistance measurements between cycling. The method was employed at IFE and resulted in limited insights to the methodology of the measurement. It is also acknowledged that this method of determining internal resistance within a half cell is very uncertain due to the large resistive interaction of the sodium metal, limiting the insight of the anode resistance within the cell. Further, a small current pulse of 1 ms may be largely attributed to the separator only, introducing additional uncertainties to the measurements. Because of this, the results was excluded from the main discussion, but presented in appendix A to act as supporting information, which could help explain some key observations.

Redox-behavior and impedance measurements

The use of $LiPF_6$ in the symmetrical cells affect the way solvents and ions react with the electrode during redox-processes compared to $NaPF_6$. The sodium ions posses different reaction rates and energy levels due to their increased mass and radius, which affect the observed results for both CV and EIS measurements. These results will therefore not depict an exact observation of what will be happening during sodiation and desodiation, but will still prove as a useful tool to compare the redox properties between the cells.

Chapter 4

Results and discussion

4.1 Structural changes after carbonization

4.1.1 Changes in surface area and particle size using BET

Treating the petroleum coke at increasing temperatures adheres to initially reduced surface area, as shown by the BET-SA presented in table 4.1. A high C-constant is linked to the adsorption process being dominated by multilayer adsorption that is typically a result of increased interaction strength between the adsorbate and adsorbent [92]. Conversely, smaller C-constant values that are observed at lower carbonization temperatures tends toward monolayer adsorption, corresponding to a weaker interaction.

Table 4.1: BET results with the BET-SA (m^2/g), C-constant and particle size distribution (PSD) (μm) for the petroleum coke samples at their calcination temperature respectively. The PSD of the untreated coke is provided to see the temperature effects on particle size relative to no heat treatment.

Sample	BET-SA	C-constant	PSD-D10	PSD-D50	PSD-D90	PSD-D95	PSD-D99
CC-untreated	-	-	5.2	12.7	23.1	30.8	34.8
CC-950	1.1744	214.929	5.4	12.3	22.1	26.6	39
CC-1100	1.0836	300.41	4.9	11.9	21.9	26.9	42.7
CC-1300	1.0803	724.78	4.8	11.8	21.7	26.7	42.4
CC-1500	1.1108	708.55	4.81	11.8	21.82	26.89	42.92

The results show that CC-950 presents a high surface area relative to the other samples, which could potentially be due to carbon-compounds in the form of strands and filaments at the surface that have not yet been scorched and expelled at this temperature. This attributes to a larger surface area and therefore explains why the adsorption relation is favored towards monolayer adsorption. The reduction of BET-SA for CC-1100 aligns with this notion, as the C-constant is increased slightly in response to this change. For CC-1300, the gas adsorption interaction is highly dominated by multilayer adsorption, believed to be a result of both a refined surface, which is indicated by the reduced BET-SA, and a slightly increased internal porosity as a result of higher temperature treatment. CC-1500 presents a small increase in surface area with slightly reduced multilayer adsorption relative to CC-1300. The exact reason for this is not known, but could be attributed to formation of open pores at the surface with introduced graphitic domains as a result of particle fusing. The presence of these domains could be aligned with the slight increase in PSD data, perhaps induced once the temperature reaches an adequate range for regional graphitization to occur. The BET C-constant is a measure of adsorbate onto the adsorbant, which includes micropores and mesopores. Therefore, it can be proposed that the shift in CC-1500 can be a result of increased microstructure, which correlates well with the trend at 1300 °C and previous research on carbonaceous materials [93], [94].

4.1.2 Crystalline properties indicated by XRD-analysis

To analyze the change in d-spacing over the course of elevated temperatures, an XRD analysis was done on four powder samples from the different petroleum coke materials. The results is presented in figure 4.1 and outlines the intensity (counts) of the diffracted radiation with respect to the diffraction angle (2θ). The three distinct peaks that are shown can be assigned to the interlayer-spacing (d002), the in-plane atomic arrangement (d100) and the higher order reflections of the d002 plane (d004) respectively [95].

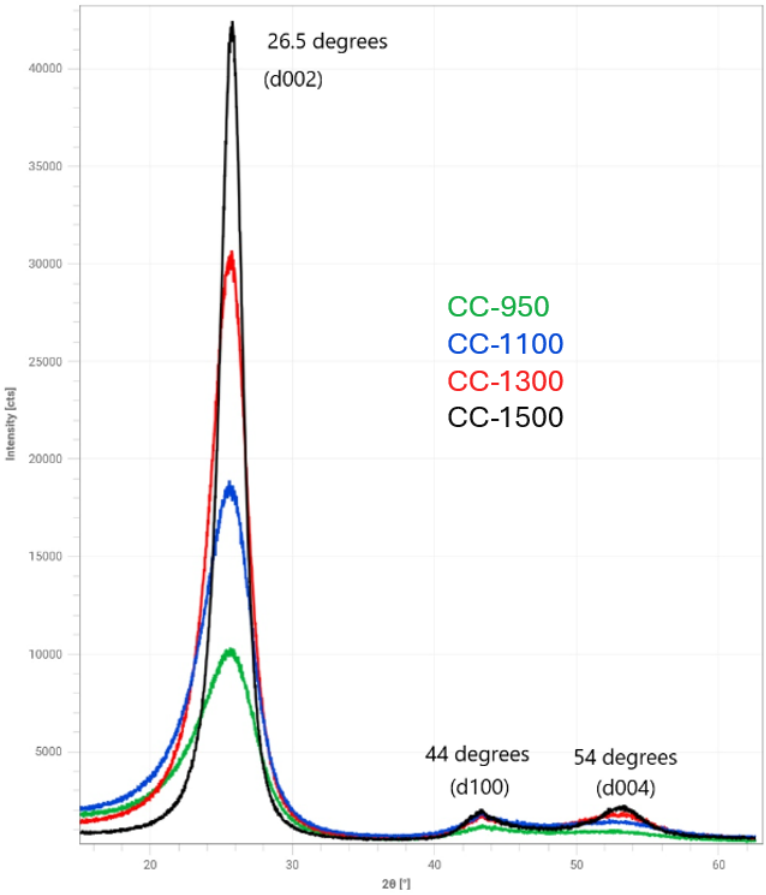

Figure 4.1: The intensity (cts) measured for the different materials at certain diffraction angles (2θ) during the XRD scan. The peaks for CC-950 (green), CC-1100 (blue), CC-1300 (red) and CC-1500 (black) are marked with their respective d-plane orientation given by Miller indices. The utilization of the divergent beam method results in no measured peak shift in the diffraction angle. The only significant change through the different samples is the increased intensity of the three materials treated above 1000 °C and the reduced width of the d002 peak for CC-1500.

The peaks corresponding to the specific planes remain at the same 2θ position regardless of the treatment temperature because of the method used. Although it is not present here, a slight peak shift can be seen for some materials treated over large temperature ranges, indicating increased/decreased d-spacing. Using Bragg's equation (2.5), the interlayer spacing corresponding to a 2θ angle of 26.5° was calculated to be approximately 0.34 nm, closely corresponding to the interlayer-spacing observed for carbon black, which is to be expected [96], [97]. The width and intensity of the peaks can be used to understand how the crystalline structure is changing over elevated temperatures. Broad peaks generally indicate smaller crystallite sizes, as small crystals results in the diffraction peaks to become broader due to the increased range of diffraction angles [98], [99]. CC-950, CC-1100 and CC-1300 shows broader peaks compared to the high temperature-treated sample at CC-1500. The increased intensity and narrowing of the peak for CC-1500 suggest a higher crystalline struc-

ture. This aligns with the typical behavior of carbon materials discussed previously, where higher temperatures facilitate graphitization, leading to more well-defined crystal structures. The degree of graphitization can be investigated further by utilizing the correct method in order to gain insights to how the d002 spacing is affected for this material.

4.1.3 Mass reduction dynamics from TGA-MS

The TGA-MS results showed no variation between the impurity contents expelled from the materials. The relative change in mass during the combustion process presented in figure 4.2 were vastly different between CC-950, CC-1100, CC-1300 and CC-1500 respectively.

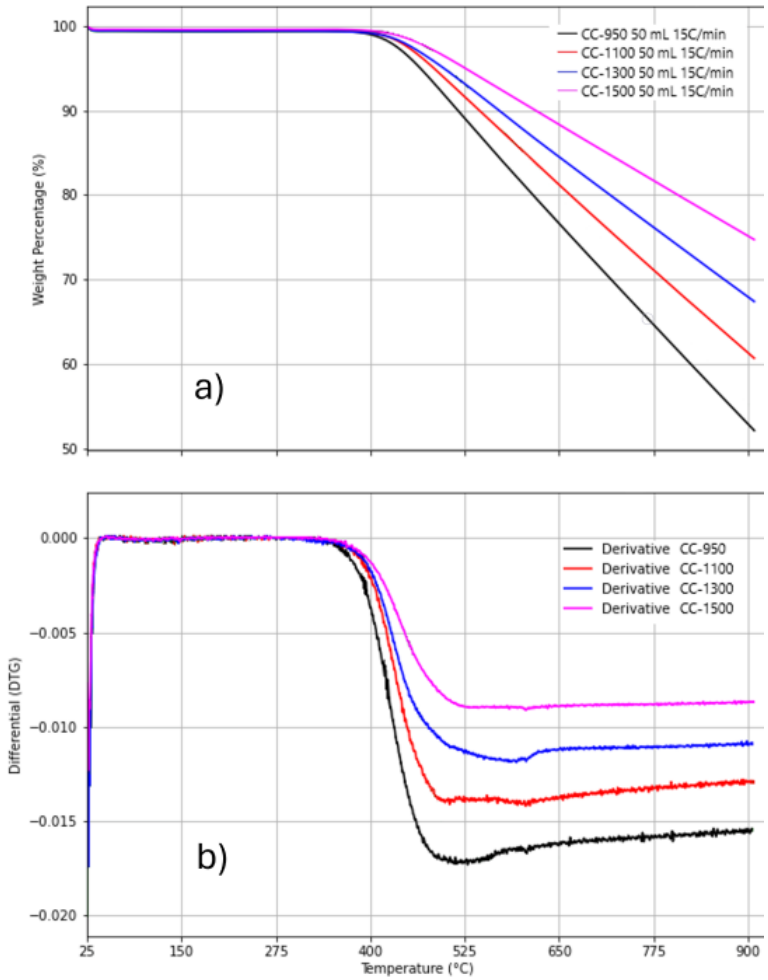

Figure 4.2: The TGA results showing a) The change in weight percentage over increasing temperature for the different materials. There is a clear indication of reduced combustion rates for materials treated at higher temperatures. b) The derivative of the curves, highlighting the respective change in mass over the same period.

The results make it clear that the petroleum coke that was treated at higher temperatures are less reactive in the combustion process during TGA. Although the reaction initiates at approximately 400°C for all samples, the entire process decreased the CC-950 weight by approximately 50%, while CC-1500 only decreased by 25%. Consequentially, all samples follow the same trend, indicating that the difference in their rate of combustion lies in the composition of the material. It is likely that this is due to the removal of carbonaceous components during elevated temperatures. At higher temperatures, the removal of functional groups lead to a porous structure with less reactive components, limiting the rate of combustion through the material. Additionally, the increased porosity might contribute to enhanced heat dispersion, lowering the active temperature in the internal regions of the

material. Lastly, the strong graphitic domains that are formed and connected through C-C and C-O-C bonds at higher calcination temperatures act as robust modifiers, increasing the energy needed to break the disorganized bonds into more refined layers. This could also attribute to reduced reactivity during combustion.

4.1.4 Visual differences indicated by SEM

Following the BET and TGA results, SEM imaging of the four materials was done at a range of magnifications in attempts to verify the discussed hypotheses. Figure 4.3 display the imaging of the powder samples at 1000x magnification.

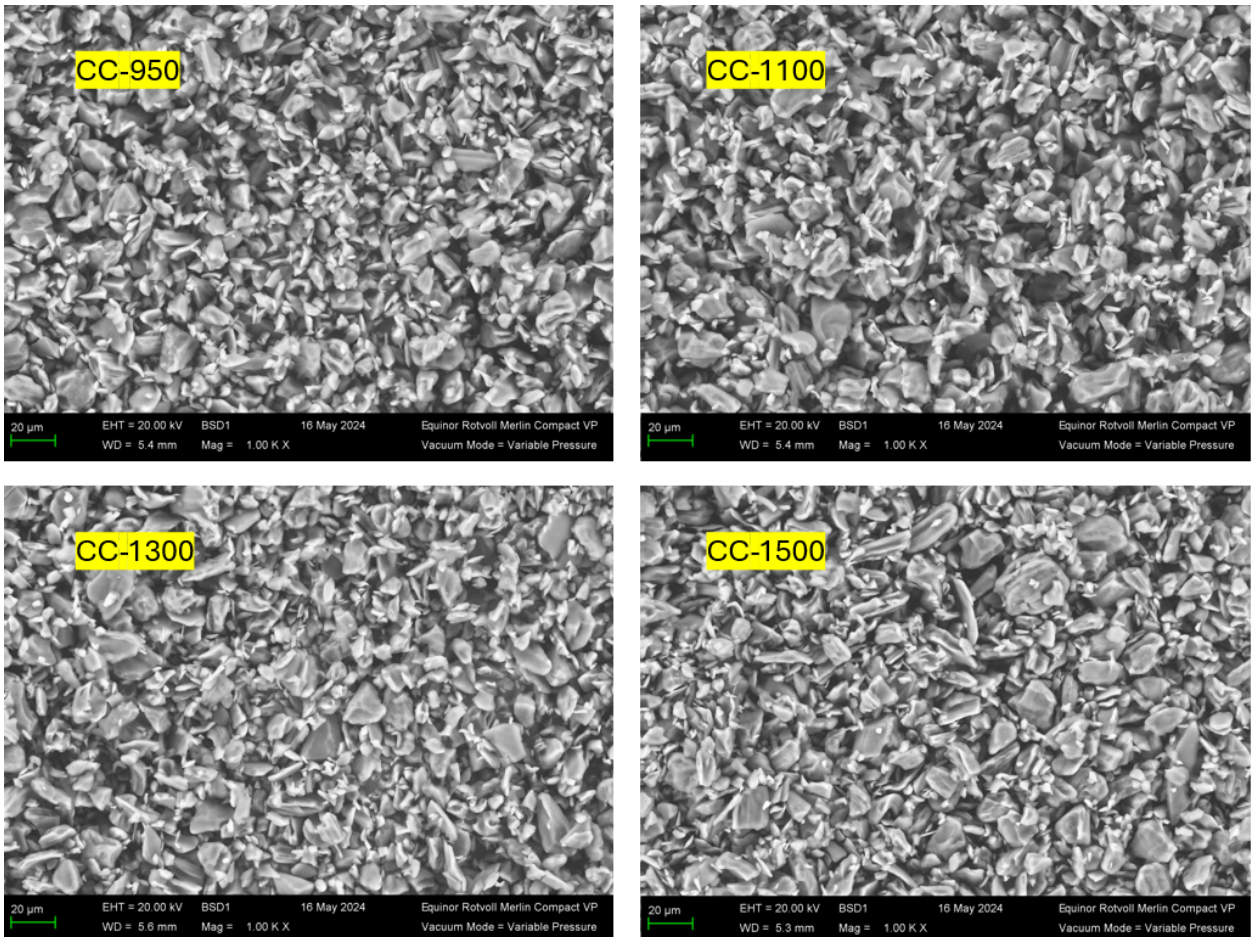

Figure 4.3: SEM imaging of the powder samples corresponding to CC-950 (top left), CC-1100 (top right), CC-1300 (bottom left) and CC-1500 (bottom right) at 1000x magnification scale. The overview image allows for the visual comparison of the particle structure following elevated treatment temperature.

The direct observation of these images presents a few noteworthy differences between the four samples. As a guide for the naked eye, a small indication of increased particle size can be made when comparing CC-950 with CC-1500. Additionally, the angular features of the particles following treatment temperatures above 1000 °C more prominently outlines the particle edges compared to CC-950, which could be connected to the increased crystallinity that was indicated by the XRD results. However, this visual interpretation could be attributed to this restricted part of the sample only, and provides limited observable differences in the particle structure between the four materials. An automated approach using analytical software tools to determine the observed particle size difference is recommended for further research to mitigate the uncertainties introduced by simply observing these results, as human error and cognitive bias may contribute to a subjective interpretation.

4.2 Electrochemical performance evaluation

The first sodiation of the half cells is analyzed in detail through a V (Na/Na^+) vs specific capacity (mAh/g) plot and a dQ/dV plot shown in figure 4.4. The plots presented in figure 4.5 provide insight to the sodiation/desodiation-behavior for the three initial cycles.

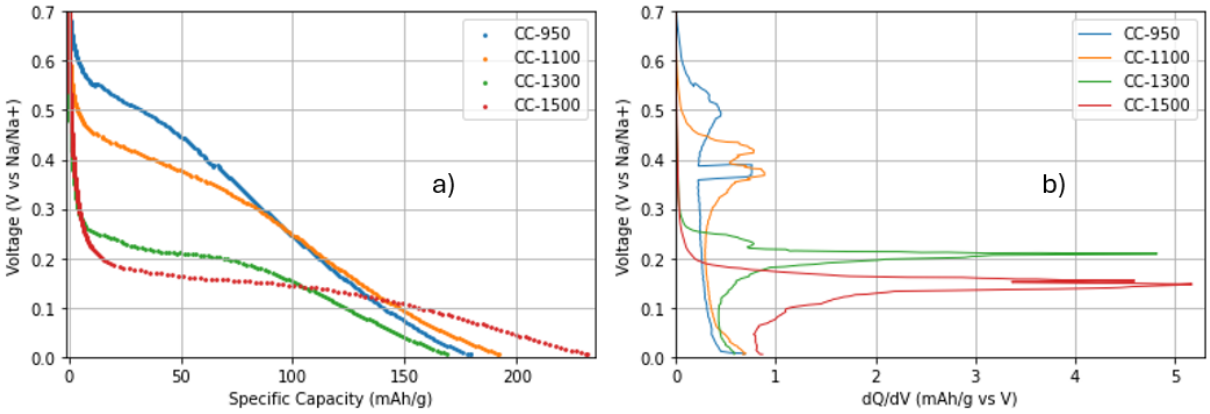

Figure 4.4: a) The comparison of the first sodiation process for CC-950 (blue), CC-1100 (orange), CC-1300 (green) and CC-1500 (red), where the reduction of sodiation potential is observed to be proportional to materials treated at higher temperatures. b) The dQ/dV plot of the same process to better visualize the intensity of the capacity change at certain votages.

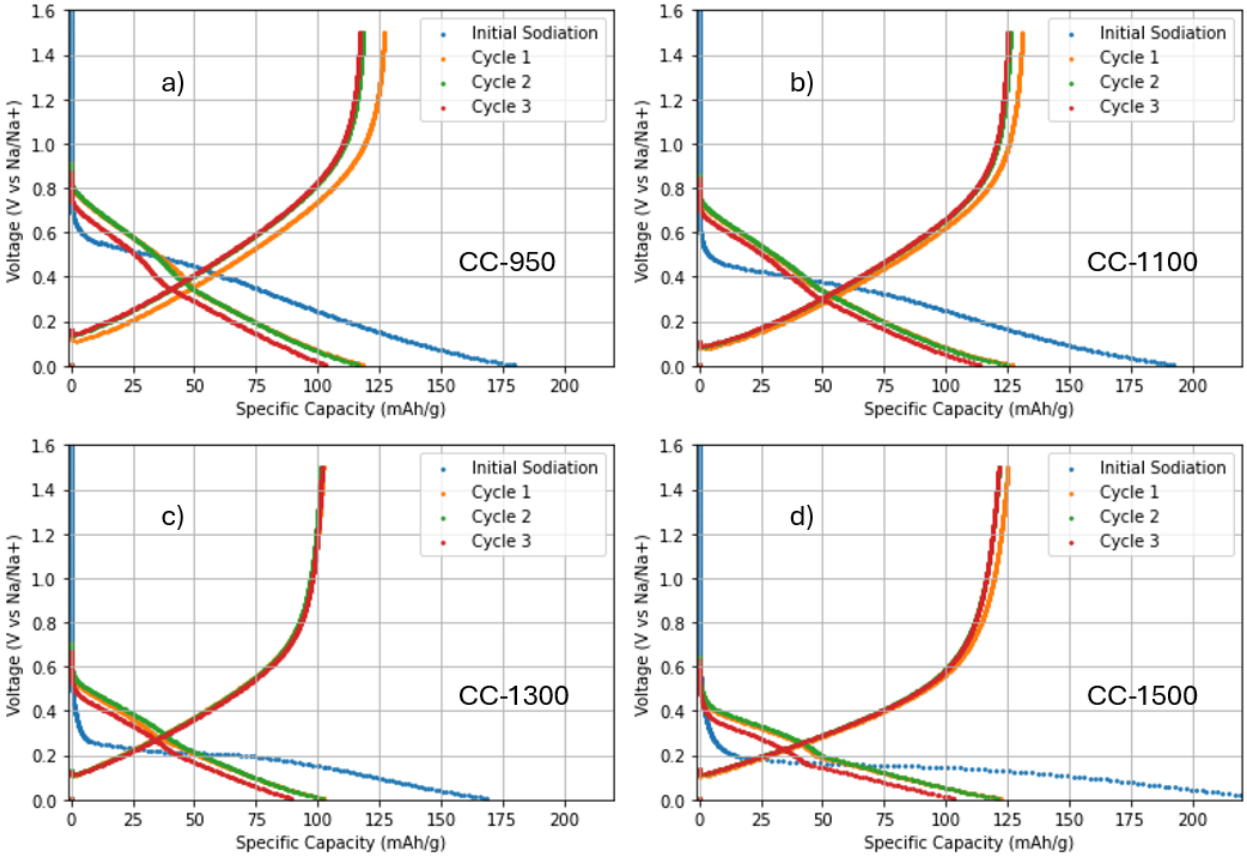

Figure 4.5: The initial sodiation (blue line), 1st cycle (orange line), 2nd cycle (green line) and 3rd cycle (red line) for the cells constructed with petroleum coke, showing the change in Specific Capacity (mAh/g) over Voltage (V vs Na/Na^+) for the materials treated at a) 950 °C b) 1100 °C c) 1300 °C and d) 1500 °C.

All cells show stable sodiation and desodiation behavior with an acceptable sodiation capacity of 103 mAh/g, 114 mAh/g, 90 mAh/g and 103 mAh/g at the end of the third cycle for CC-950, CC-1100, CC-1300 and CC-1500 respectively. Although CC-1300 presents slightly reduced sodiation capacity compared to the other cells, it contains the least amount of hysteresis during sodiation and desodiation, indicating reduced irreversible processes. The observed sodiation voltages (0.55 V, 0.45 V, 0.25 V, and 0.18 V) at the initial sodiation cycle indicate that the sodiation process starts at lower potentials for the petroleum coke treated at higher temperatures. This suggests that the coke treated at higher temperatures exhibits improved sodiation kinetics, as surface refinement and pore accessibility could facilitate easier transport of sodium into the carbon structure at lower potentials. This is highlighted by the dQ/dV plot, where a significant portion of the change in capacity is assigned to the lower voltage levels for CC-1300 and CC-1500 compared to CC-950 and CC-1100. Notably, the sodiation process in the following cycles is occurring at higher voltages due to the formation of SEI at the surface, which introduce additional resistance for sodium to intercalate. This is also the reason for the reduced specific capacity measured at the 2nd and 3rd sodiation cycle, as initial SEI formation occupy physical space on the surface, reducing the reactive surface area composed of active sites available for sodium storage in the subsequent cycles.

The transition from an S-shaped curve at higher potentials for CC-950 to a flat L-shaped curve at lower potentials for CC-1500 in the initial sodiation step suggested improved intercalation kinetics with rising calcination temperatures. To validate these results, the sloping capacity (above 0.1V) and plateau capacity (below 0.1 V) for the third cycle was analyzed. At this stage, the majority of the initial SEI formation should be complete, allowing the capacity to be assigned to the intercalation mechanisms. Table 4.2 refers to the change in the contribution of sloping and plateau capacity that was measured during the third cycle.

Table 4.2: The sloping capacity (capacity measured above 0.1 V (S_{cap})) and plateau capacity (capacity measured below 0.1 V (P_{cap})) recorded from the third cycle for each cell. The P_{cap} contribution refers to the percentage of capacity that is attributed to the plateau voltage region with respect to the total sodiation capacity.

Sample	S_{cap}(mAh/g)	P_{cap}(mAh/g)	P_{cap} contribution
CC-950	83	20	19%
CC-1100	88	26	23%
CC-1300	65	25	28%
CC-1500	65	38	37%

It was found that the plateau capacity contribution gradually increase in proportion to higher calcination temperature. The initial plateau capacity contributed 19 % of the total measured sodiation capacity for CC-950 and 37% for CC-1500.

In similar work, Shen Qiu, et al provides experimental evidence to conclude that this change in plateau capacity contribution comes from sodium insertion within the graphene layers, which was also found several other studies [22], [29], [30], [100]–[102]. Although measurements at higher calcination temperatures are lacking, the notion of increased crystallinity, porosity and sloping capacity at 1500 °C strongly suggests that regional graphitization effects are occurring. Further investigation of this relationship at higher calcination temperatures is therefore recommended to get a better overview of this effect.

4.2.1 Density and porosity changes following heat treatment

The density, porosity and closed pore volume of the electrodes from equations (2.3), (2.4) and (2.6) was calculated using the capacity from the cycling results. Figure 4.6 presents the comparison of the calculated density to porosity and the pore volume contribution for the electrodes with a ± 5% error margin to account for uncertainty regarding thickness measurements.

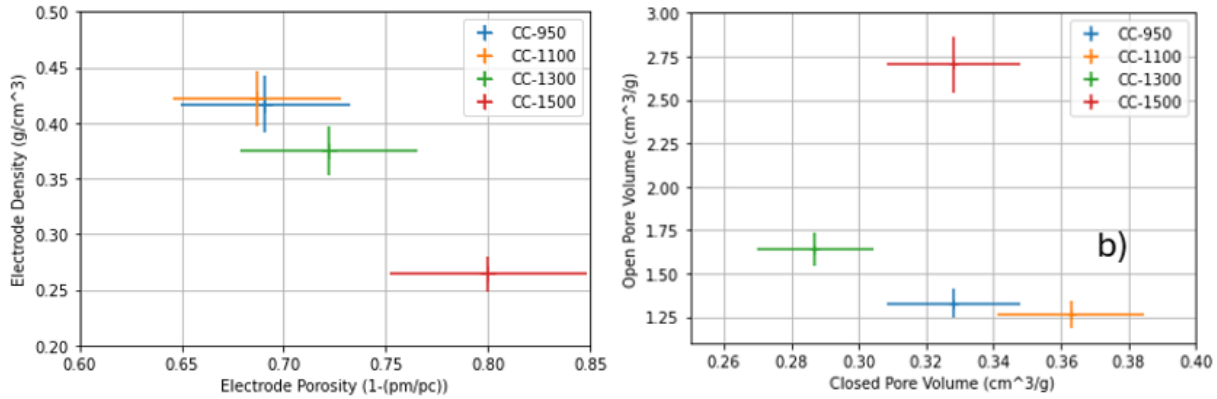

Figure 4.6: a) The respective density and porosity comparison of the electrodes constructed with the different materials as a result of temperature treatment with 5% error margin. b) The comparison of open and closed pore volume in the electrodes with 5% error margin.

From these results, it is clear that the density and porosity are inversely related, which is to be expected. This inverse relationship helps explain observed the variation in mass loading during half-cell construction. Naturally, the estimation of open pore volume is higher for materials with greater porosity. This increase in porosity is accompanied by more voids, as a result from the reduction in active material density due to the heat treatment of the material, which exfoliate impurities.

The closed pore volume was calculated to be 0.328, 0.363, 0.287, and 0.328 cm^3/g for CC-950, CC-1100, CC-1300, and CC-1500, respectively. This suggests that the closed pore volume remains relatively constant through most of the heat treatment process. The decrease in closed pore volume observed at 1300 °C could indicate some form of structural collapse. A study by Li et al. found that a decrease in closed pore volume was associated with decreased reversible capacity in porous hard carbon materials [23]. The discussed intercalation mechanism related to pore filling and adsorption in the carbon layers around closed pores could help explain this behavior. However, the slight reduction in this single sample is not enough evidence for this to be a conclusive explanation. Further complementary work is therefore needed to verify this relation.

4.2.2 SEI formation and Coulombic efficiency

Another aspect that is worth discussing is the SEI formation during the initial cycles and the CE over prolonged cycling. Like the plateau capacity, the capacity percentage assigned to the formation of SEI for the three initial cycles was found to be increasing with elevated temperature. By using equation (2.2), the SEI formation during the three initial formation cycles resulted in 12.5%, 14%, 18.3% and 22.5% uptake of the total capacity for CC-950, CC-1100, CC-1300 and CC-1500 respectively. The increased SEI formation could be attributed to a more homogeneous surface as a result of elevated temperatures, as mentioned in section 2.2.3, creating a uniform layer across the surface with equal thickness [103]. Additionally, the increase of open pore volume as discussed previously, might introduce additional reactive

sites for the formation of SEI to occur at the carbon surface.

While the majority of SEI formation occurs during the initial cycles, additional SEI may form over prolonged cycling in unprotected regions as a result of inhomogeneous formation. Figure 4.7 presents the measured Coulombic efficiency over the course of 50 cycles.

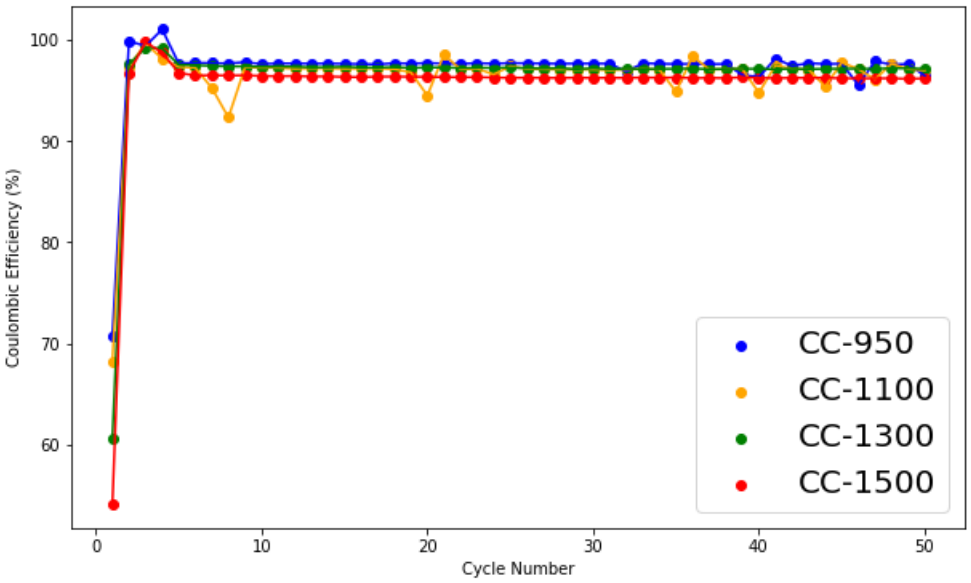

Figure 4.7: The Coulombic efficiency (%) presented for each cell over the course of 50 cycles. The low CE at the first cycle is assigned to the formation of SEI, which can be seen to decrease in proportion to higher treatment temperatures.

The initial CE was calculated to be approximately 71 %, 68 %, 60 % and 54 % for CC-950, CC-1100, CC-1300 and CC-1500 respectively. This decrease in proportion to increased treatment temperature alligns with the theory, where a homogeneous surface with additional reactive carbon sites is found to contribute to additional SEI formation. The following three cycles are observed to be close to 100 % for all cells. This is assumed to be due to the dissolution of stored sodium from the previous cycle, as incomplete SEI formation can sometimes trap sodium atoms during formation, only for them to be released during a later cycle [104], [105]. This is measured as additional capacity, and can be seen in the CE fluctuations for CC-1100 during cycling. Because of this notion, the measured CE at an average of 97 % for all cells for 50 ongoing cycles should be taken with caution, as the continuous dissolution and formation of the SEI layer might affect these results. The overlap between the cells still indicate similar CE characteristics for all cells, rendering all materials with their respective carbonization temperature adequate for sodium use.

Based on the internal resistance measurements of CC-1500 from table A.1 in appendix A, it could be suggested that a majority of the SEI formation which is initially thought to occur at the surface and within pores, leave some regions exposed without adequate protection. Over time, this could result in electrolyte diffusion through exposed areas. This is by no means confirmed by the results, but could invite the incentive to further investigate the materials during prolonged cycling in full-cell configurations to clarify if the SEI formation is sufficient.

4.2.3 Redox-behavior through CV analysis

To get an indication of the redox reactions at the surface, a CV analysis was conducted on the symmetrical cells. Figure 4.8 presents the measured current response (mA) at the given cell voltage (Ewe/V Vs. SCE).

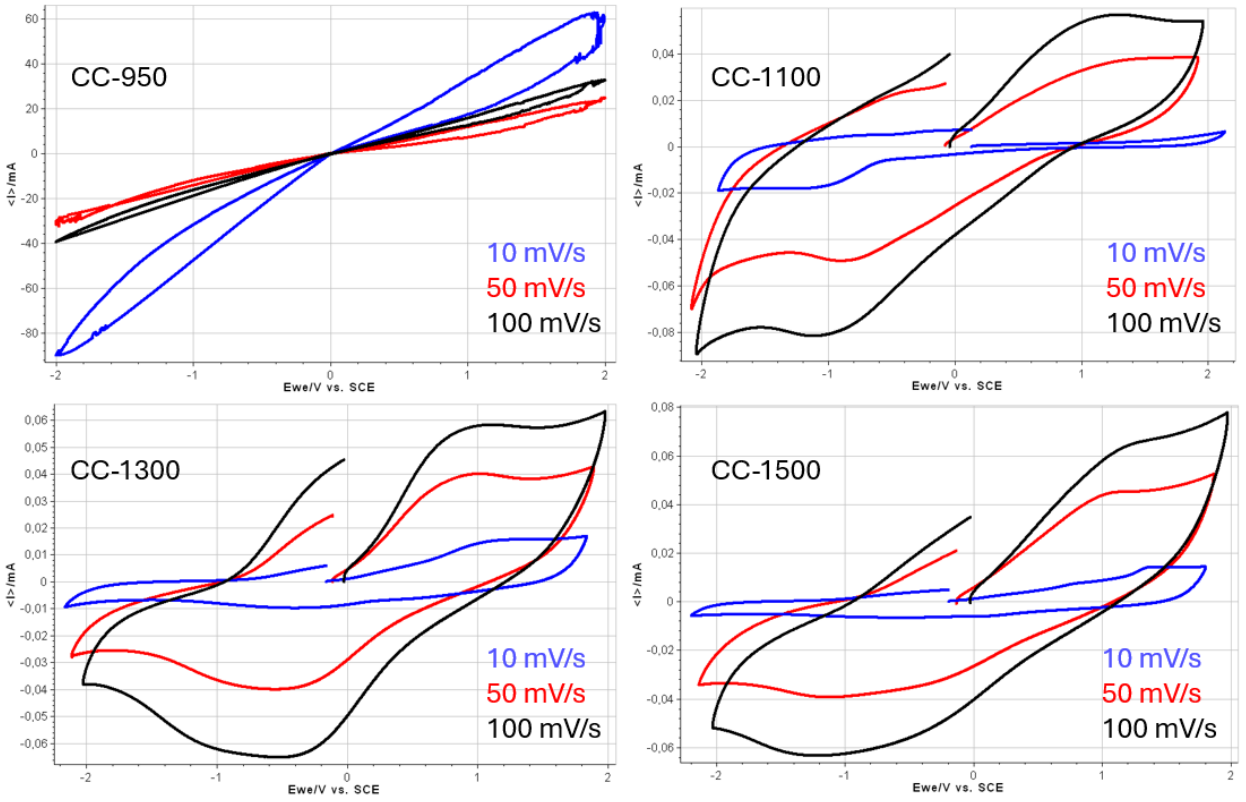

Figure 4.8: The CV of the symmetrical cells constructed with the different materials and the corresponding scan rates at 10 mV/s, 50 mV/s and 100 mV/s. The shift in start and end positions between the scan rates is present because the scans were done in succession to another. The cell voltage experiencing delayed reactions during the scans corresponded to a shift in the observed CV plots.

CC-950 presents no apparent redox pairs like the remaining cells, but rather a purely resistive behavior corresponding to a linearly-reversible curve that peaks at high currents between 20 and 90 mA. This could be due to a short circuit, either from puncturing the separator during compression, or significant movement of the internal parts of the cell during construction, causing direct contact between the electrodes. Although a short circuit is the most plausible explanation for this behavior, the lowest scan rate of 10 mV/s shows the highest current peaks with introduced hysteresis. According to theory, this should not be the case, as the current would scale linearly and proportionally with increased voltage in a short circuit scenario. This odd behavior was found in both symmetrical cells when performing the CV analysis. Regardless, the significant increase in current and deviation in its curve behavior, makes CC-950 incomparable to the other cells for this analysis.

Materials treated at higher temperatures present more expected current amplitudes. In principle, symmetrical cells should not exhibit any faradaic reactions, where instead a purely capacitive behavior with rectangular CV curves would be observed. The faradaic reactions observed is likely due to the $LiPF_6$ salt and solvents reacting with the electrode surface, giving rise to redox reactions. The peak currents and the capacitive nature of the curves become more pronounced at higher scan rates, which is expected due to relationship between scan rate and peak currents. The presence of these reactions therefore suggests that the electrode

made from petroleum coke is not purely capacitive, but posses charge transfer properties at the surface of the electrode. Interesting research on faradaic reactions connect some of the observed reactions in the CV plots to pseudocapacitance, which arises from ion adsorption onto the electrode surface through reversible redox reactions [106]. For carbon materials, these reactions are directly linked to the rich functional groups present on the surface, which could help explain the observed curve behavior [107]. By further testing these materials in symmetrical-cell configurations, the notion of pseudocapacitive reactions in petroleum coke anodes can be determined, presenting new insights on the electrochemical properties of this material.

4.2.4 Impedance measurements through EIS

These results are further related to the impedance at the electrode surface, shown by figure 4.9. The EIS measurements was performed on the same symmetrical cells used in the CV analysis.

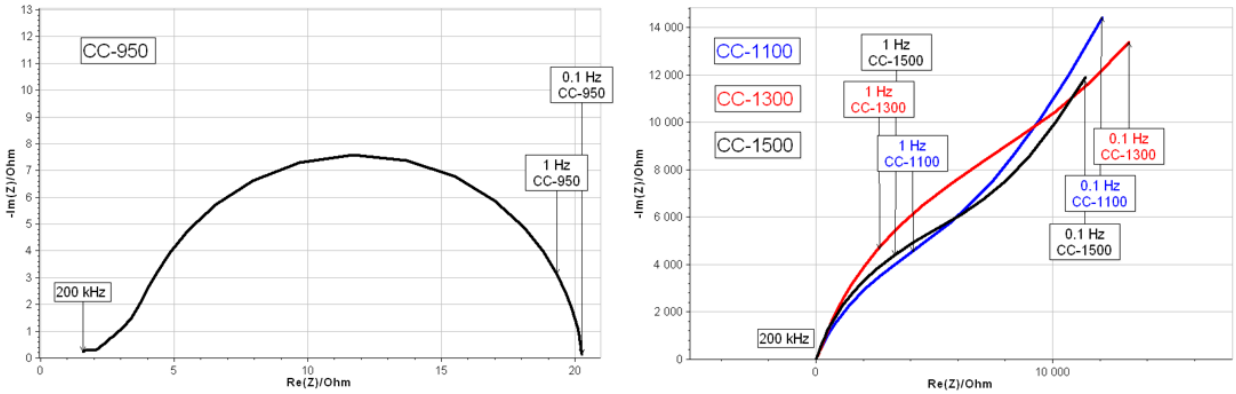

Figure 4.9: EIS measurements in a Nyquist representation with 200 kHz, 1 Hz and 0.1 Hz marked as a guide for the eye. The CC-950 symmetrical cell (left) is shown to only posses a semi-circle in its curve. CC-1100, CC-1300 and CC-1500 (right) show a large capacitive branch in the form of a distorted 45 ° line for all cells.

The Nyquist plot containing CC-950 affirms the abnormal behavior observed in the CV results. The initial suspicion towards a short circuit could be affirmed further here, as the semi-circle resembling the charge transfer resistance is very low. Moreover, there is limited impedance at lower frequencies, resulting in no capacitive branch extension which would be expected for these symmetrical cells. However, both of the symmetrical cells showed this abnormal charge transfer resistance, as shown in figure A.1 in appendix A. While there could be a short circuit for both cells, this is relatively unlikely given that all other cells were giving adequate results. Without becoming too speculative, the anomaly remains unsolved, and nulls the comparative approach that was supposed to be made towards the other cells.

There is however a significant increase in imaginary impedance at low frequencies for cells treated at higher temperatures, suggesting high capacitive storage properties. The expected curve behavior for a symmetrical cell with electrolyte containing ions should be a sharp transmission line model shape with a 45 ° line, followed by increasing imaginary impedance values once the frequency is lowered. However, this prominently described figure is not present here, where instead the capacitive branch acts distorted. This could be linked to the faradaic reactions that were observed in the CV analysis, causing the expected behavior to deviate as a result of occurring redox reactions. While all the remaining cells indicate good capacitive behavior, the comparative difference shows that elevated temperature treatment results in slightly reduced capacitive behavior, while also slightly reducing the charge transfer resistance for CC-1500.

Chapter 5

Conclusive remarks

During this thesis, a theoretical framework of the working principles in using petroleum coke as an anode for SIBs has been presented. The main intercalation mechanisms of sodium in porous carbon has been discussed, followed by an explanation of the structural properties involved in porous carbon. Moreover, the thesis delves into the nuanced relationship between the electrode-electrolyte interface, solid-electrolyte interface and the effects of carbonization temperatures, followed by an overview of the graphtization degree that occurs in carbonaceous materials. Instrumental methods of analysis is covered through a descriptive part on BET theory, CV analysis and the EIS technique, providing the reader with foundational knowledge required to follow the discussion of the results.

A material synthesis was performed, where the petroleum coke powder was treated at temperatures of 950 °C, 1100 °C, 1300 °C and 1500 °C to cover the entire range of high carbonization temperatures. Several material analysis methods was then used to characterize the materials through properties like surface area determination, crystallinity degree and porosity calculations. The materials was then electrochemically tested to evaluate a link between the carbonization temperatures and electrochemical performance in SIBs.

The surface area of the materials was found to initially decrease with increasing temperature treatment of up to 1300 °C. At 1500 °C, the surface area increased slightly relative to the material treated at 1300 °C with a small increase in particle size, indicated by the BET results. This could further be seen in a visual representation of the four materials through SEM imaging at 1000x magnification, where the materials calcined above 1000 °C had more prominently outlined angular features opposed to the material treated at 950 °. The visual comparison between the materials treated at 950 °C and 1500 °C did to an extent help verify the increase in large particle size at higher temperatures. This was however done without an analytical software, introducing uncertainties regarding human error and cognitive bias. The notion of angular features gathered from the SEM results was further affirmed through the XRD analysis, where an increase in crystalline structure could be observed at elevated temperature treatment through increased peak intensities. Additionally, the material treated at 1500 °C had less peak broadening than all the other materials, further implying that regional graphitization effects could be occurring at this temperature. TGA was performed on the samples in a oxygen rich atmosphere, facilitating mass reduction dynamics based on combustion at 900 °C. Here it was found that the mass-reduction rate was reduced for materials with increasing temperature treatment, as a result of reduced impurity contents and reactive components that have been expelled during elevated temperatures.

The electrochemical capacity at the end of the third cycle was found to be 103 mAh/g, 114 mAh/g, 90 mAh/g and 103 mAh/g for CC-950, CC-1100, CC-1300 and CC 1500 respectively, indicating adequate sodium storage within all the materials after SEI formation. The initial sodiation voltage was reduced with respect to the materials treated at higher

temperatures, suggesting improved sodiation kinetics through surface refinement and pore accessibility. This was further confirmed by the measured voltage plateau capacities, which corresponded to 19 %, 23 %, 28 % and 37 % of the total sodiation for CC-950, CC-1100, CC-1300 and CC-1500 respectively. Based on similar studies, this could be attributed to the increased crystallinity and porosity that was found in the materials treated at higher temperatures, increasing the availability of active sites within pores and graphitic domains. However, further work within an extended temperature range (500 °C - 2000 °C) could help validate these results. The SEI formation resulted in consuming 12.5 %, 14 %, 18.3 % and 22.5 % of the total capacity during the three initial formation cycles for CC-950, CC-1100, CC-1300 and CC-1500 respectively. This increase can be assigned to the increased porosity and notion of a refined material surface with elevated temperature treatment, introducing additional reactive sites for the formation of SEI to occur. The Coulombic efficiency stayed relatively stable at approximately 97 % for all cells over the course of 50 cycles. Some fluctuations in CE was found, suggesting the dissolution and reformation of SEI components that initially trap sodium atoms which is then released at a later cycle. The redox reactions was analyzed using CV analysis on symmetrical cells made from each material. The CC-950 cells presented abnormal behavior, which initially seemed like a short circuit. The other cells presented some form of faradaic reactions which was assigned to charge transfer at the surface given the used electrolyte containing ions. Additionally, the EIS measurements that was conducted on the same cells presented a small charge transfer resistance with no capacitive behavior for CC-950, affirming the abnormal behavior observed in the CV plots. Given the lack of supplementary data as there was no material leftover to create new cells, the cause of this remains unknown. The remaining cells showed good capacitive behavior, although a distorted version of the expected transmission line model shape was presented. This could be linked ti the faradaic reactions that were observed in the CV analysis. The comparative difference between the cells showed that elevated temperature treatment resulted in a small reduction in capacitive behavior, while also reducing the charge transfer resistance slightly for the material treated at 1500 °C.

The combined results indicate that while all materials are adequate for use in SIBs, they present certain differences in material structure that affects the electrochemical performance of the cells in different ways. Additional analysis is therefore needed to establish the direct implications of these differences, to be able to apply the correct temperature treatment of the material to certain energy storage applications for optimized electrochemical performance.

Future work

All of the results presented in this work will be further complemented by conducting a similar line of experiments on petroleum coke treated in the extended temperature range of 500 °C - 2000 °C and beyond. Additional XRD measurements should be employed, using the correct method to determine the change in d002-spacing between the graphene layers that occur during elevated temperature treatment. By further testing petroleum coke in a full-cell configuration with a sodium based anode like $NaCoO_2$, one can more accurately reflect how the observed differences in the petroleum coke affect electrochemical performance. Additional CV and EIS measurements should be employed for the petroleum coke treated at 950 °C to correctly assess the symmetric-cell properties of CC-950, which were lacking in this report. To get additional insights into the internal structure of the petroleum coke, Raman spectroscopy should be utilized in coexistence with thes analysis presented in this work. This will validate the results further, and could contribute to new insights in using petroleum coke as an anode material for SIBs.

Acknowledgements

I would first and foremost like to thank my two supervisors Børre Tore Børresen from Equinor and Johannes Martin Landesfeind from UiA, for their collaboration during the last two semesters. You have provided me with the possibility of pursuing research within the battery field, and have assisted with the experimental troubles that have occurred, essentially making this thesis possible. This has funneled my increasing interest in the field, and have allowed me to familiarize myself within research methodologies with such motivation. I truly wish for the best in your future careers, and I really do hope our paths cross again.

I would also like to thank Gunstein Skomedal from Vianode for lending a hand regarding the milling and BET analysis of the petroleum coke. Thank you to Odin Kvam and my fellow student Kristoffer Klausen for providing assistance with running the TGA-MS experiments as well as interpreting the results. Additional thanks to Carl Erik Lie Foss and Theresa Nguyen at IFE for allowing me to visit their research facility to construct my sodium cells, and for their insights into electrochemistry during my visit. Thank you to Fazilet Guerer for helping me conduct the XRD analysis. And lastly, thanks to the Battery coast team at UiA & Morrow for allowing me to use their laboratory equipment with such ease.

Appendix A

Datasheet A

The internal resistance (R) measurements during cycling is presented in table A.1.

Table A.1: The internal resistance (Ω) that was measured in all cells after sodiation for a total of 50 cycles.

Sample	1st R (Ω)	5th R (Ω)	10th R (Ω)	20th R (Ω)	35th R (Ω)	50th R (Ω)
CC-950	267	245	224	196	180	159
CC-1100	193	46	37	40	44	48
CC-1300	203	81	85	75	68	75
CC-1500	147	56	61	67	91	132

The internal resistance measurements reveal notable variations in the sodiation processes among the different samples. Following the formation of SEI, CC-950 exhibits a marginal decrease in resistance compared to the other cells.

In contrast, CC-1100 demonstrates the lowest internal resistance which is inherently stable over prolonged cycling. The increased resistance at the 35th and 50th cycle for CC-1500 may be directly attributed to SEI formation in the porous structure and at graphitic domains, as the electrode is exposed to further electrolyte decomposition due to unprotected regions from the SEI layer, allowing the diffusion of electrolyte components to reach the electrode.

The EIS measurement of the 2nd CC-950 symmetrical cell is shown in figure A.1.

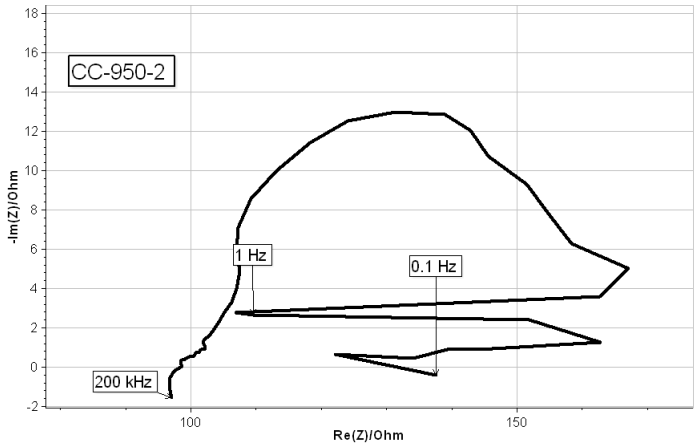

Figure A.1: The 2nd symmetrical cell of CC-950 with 200 kHz, 1 Hz and 0.1 Hz marked as a guide for the eye.

Oddly, this cell presents a similar abnormal behavior much like the first cell, presenting a clear charge transfer resistance with no capacitive branch to follow.

Bibliography

[1] J. H. McClendon, "Elemental abundance as a factor in the origins of mineral nutrient requirements," *Journal of Molecular Evolution*, vol. 8, no. 2, pp. 175–195, 1976, ISSN: 1432-1432. DOI: 10.1007/BF01739102.

[2] M. Chen, Q. Liu, S.-W. Wang, E. Wang, X. Guo, and S.-L. Chou, "High-abundance and low-cost metal-based cathode materials for sodium-ion batteries: Problems, progress, and key technologies," *Advanced Energy Materials*, vol. 9, no. 14, p. 1 803 609, 2019. DOI: https://doi.org/10.1002/aenm.201803609.

[3] M. I. Jamesh and A. Prakash, "Advancement of technology towards developing na-ion batteries," *Journal of Power Sources*, vol. 378, pp. 268–300, 2018, ISSN: 0378-7753. DOI: https://doi.org/10.1016/j.jpowsour.2017.12.053.

[4] J. Tang, A. D. Dysart, and V. G. Pol, "Advancement in sodium-ion rechargeable batteries," *Current Opinion in Chemical Engineering*, vol. 9, pp. 34–41, 2015, ISSN: 2211-3398. DOI: https://doi.org/10.1016/j.coche.2015.08.007.

[5] W. Lu, Z. Wang, and S. Zhong, "Sodium-ion battery technology: Advanced anodes, cathodes and electrolytes," *Journal of Physics: Conference Series*, vol. 2109, no. 1, p. 012 004, 2021. DOI: 10.1088/1742-6596/2109/1/012004.

[6] Y. Wen, K. He, Y. Zhu, *et al.*, "Expanded graphite as superior anode for sodium-ion batteries," *Nature Communications*, vol. 5, no. 1, p. 4033, 2014. DOI: 10.1038/ncomms5033.

[7] L. Xiao, H. Lu, Y. Fang, *et al.*, "Low-defect and low-porosity hard carbon with high coulombic efficiency and high capacity for practical sodium ion battery anode," *Advanced Energy Materials*, vol. 8, no. 20, p. 1 703 238, 2018. DOI: https://doi.org/10.1002/aenm.201703238.

[8] E. Irisarri, A. Ponrouch, and M. R. Palacin, "Review—hard carbon negative electrode materials for sodium-ion batteries," *Journal of The Electrochemical Society*, vol. 162, no. 14, A2476, 2015. DOI: 10.1149/2.0091514jes.

[9] D. A. Stevens and J. R. Dahn, "High capacity anode materials for rechargeable sodium-ion batteries," *Journal of The Electrochemical Society*, vol. 147, no. 4, p. 1271, 2000. DOI: 10.1149/1.1393348.

[10] Z. Li, C. Bommier, Z. S. Chong, *et al.*, "Mechanism of na-ion storage in hard carbon anodes revealed by heteroatom doping," *Advanced Energy Materials*, vol. 7, no. 18, p. 1 602 894, 2017. DOI: https://doi.org/10.1002/aenm.201602894.

[11] Q. Jin, K. Wang, P. Feng, Z. Zhang, S. Cheng, and K. Jiang, "Surface-dominated storage of heteroatoms-doping hard carbon for sodium-ion batteries," *Energy Storage Materials*, vol. 27, pp. 43–50, 2020, ISSN: 2405-8297. DOI: https://doi.org/10.1016/j.ensm.2020.01.014.

[12] R. Alcántara, J. M. J. Mateos, and J. L. Tirado, "Negative electrodes for lithium- and sodium-ion batteries obtained by heat-treatment of petroleum cokes below 1000°c," *Journal of The Electrochemical Society*, vol. 149, no. 2, A201, 2002. DOI: 10.1149/1.1431963.

[13] Y. Miao, J. Zong, and X. Liu, "Phosphorus-doped pitch-derived soft carbon as an anode material for sodium ion batteries," *Materials Letters*, vol. 188, pp. 355–358, 2017, ISSN: 0167-577X. DOI: https://doi.org/10.1016/j.matlet.2016.11.110.

[14] S.-W. Kim, D.-H. Seo, X. Ma, G. Ceder, and K. Kang, "Electrode materials for rechargeable sodium-ion batteries: Potential alternatives to current lithium-ion batteries," *Advanced Energy Materials*, vol. 2, no. 7, pp. 710–721, 2012. DOI: https://doi.org/10.1002/aenm.201200026.

[15] E. Heintz, "The characterization of petroleum coke," *Carbon*, vol. 34, no. 6, pp. 699–709, 1996, ISSN: 0008-6223. DOI: https://doi.org/10.1016/0008-6223(96)00037-1.

[16] M. Legin-Kolar, A. Rađenović, and D. Ugarković, "Changes in structural parameters of different cokes during heat treatment to 2400°c," *Fuel*, vol. 78, no. 13, pp. 1599–1605, 1999, ISSN: 0016-2361. DOI: https://doi.org/10.1016/S0016-2361(99)00083-6.

[17] X. Xiang, K. Zhang, and J. Chen, "Recent advances and prospects of cathode materials for sodium-ion batteries," *Advanced Materials*, vol. 27, no. 36, pp. 5343–5364, 2015. DOI: https://doi.org/10.1002/adma.201501527.

[18] J. Qian, C. Wu, Y. Cao, *et al.*, "Prussian blue cathode materials for sodium-ion batteries and other ion batteries," *Advanced Energy Materials*, vol. 8, no. 17, p. 1 702 619, 2018. DOI: https://doi.org/10.1002/aenm.201702619.

[19] M. D. Slater, D. Kim, E. Lee, and C. S. Johnson, "Sodium-ion batteries," *Advanced Functional Materials*, vol. 23, no. 8, pp. 947–958, 2013. DOI: https://doi.org/10.1002/adfm.201200691.

[20] N. Yabuuchi, K. Kubota, M. Dahbi, and S. Komaba, "Research development on sodium-ion batteries," *Chemical Reviews*, vol. 114, no. 23, pp. 11 636–11 682, 2014, ISSN: 0009-2665. DOI: 10.1021/cr500192f.

[21] N. Sun, J. Qiu, and B. Xu, "Understanding of sodium storage mechanism in hard carbons: Ongoing development under debate," *Advanced Energy Materials*, vol. 12, no. 27, p. 2 200 715, 2022. DOI: https://doi.org/10.1002/aenm.202200715.

[22] S. P. Ong, V. L. Chevrier, G. Hautier, *et al.*, "Voltage, stability and diffusion barrier differences between sodium-ion and lithium-ion intercalation materials," *Energy Environ. Sci.*, vol. 4, pp. 3680–3688, 9 2011. DOI: 10.1039/C1EE01782A.

[23] Y. Li, Y. Lu, Q. Meng, *et al.*, "Regulating pore structure of hierarchical porous waste cork-derived hard carbon anode for enhanced na storage performance," *Advanced Energy Materials*, vol. 9, no. 48, p. 1 902 852, 2019. DOI: https://doi.org/10.1002/aenm.201902852.

[24] D. Guerard and A. Herold, "Intercalation of lithium into graphite and other carbons," *Carbon*, vol. 13, no. 4, pp. 337–345, 1975, ISSN: 0008-6223. DOI: https://doi.org/10.1016/0008-6223(75)90040-8.

[25] Z. X. Shu, R. S. McMillan, and J. J. Murray, "Electrochemical intercalation of lithium into graphite," *Journal of The Electrochemical Society*, vol. 140, no. 4, p. 922, 1993. DOI: 10.1149/1.2056228.

[26] P. Thomas and D. Billaud, "Electrochemical insertion of sodium into hard carbons," *Electrochimica Acta*, vol. 47, no. 20, pp. 3303–3307, 2002, ISSN: 0013-4686. DOI: https://doi.org/10.1016/S0013-4686(02)00250-5.

[27] M. Anji Reddy, M. Helen, A. Groß, M. Fichtner, and H. Euchner, "Insight into sodium insertion and the storage mechanism in hard carbon," *ACS Energy Letters*, vol. 3, no. 12, pp. 2851–2857, 2018. DOI: 10.1021/acsenergylett.8b01761.

[28] M. P. Mercer, S. Affleck, E. M. Gavilán-Arriazu, *et al.*, "Sodiation of hard carbon: How separating enthalpy and entropy contributions can find transitions hidden in the voltage profile," *ChemPhysChem*, vol. 23, no. 5, e202100748, 2022. DOI: https://doi.org/10.1002/cphc.202100748.

[29] S. Qiu, L. Xiao, M. L. Sushko, *et al.*, "Manipulating adsorption–insertion mechanisms in nanostructured carbon materials for high-efficiency sodium ion storage," *Advanced Energy Materials*, vol. 7, no. 17, p. 1 700 403, 2017. DOI: https://doi.org/10.1002/aenm.201700403.

[30] S. Alvin, H. S. Cahyadi, J. Hwang, W. Chang, S. K. Kwak, and J. Kim, "Revealing the intercalation mechanisms of lithium, sodium, and potassium in hard carbon," *Advanced Energy Materials*, vol. 10, no. 20, p. 2 000 283, 2020. DOI: https://doi.org/10.1002/aenm.202000283.

[31] H. Hou, X. Qiu, W. Wei, Y. Zhang, and X. Ji, "Carbon anode materials for advanced sodium-ion batteries," *Advanced Energy Materials*, vol. 7, no. 24, p. 1 602 898, DOI: https://doi.org/10.1002/aenm.201602898.

[32] Y. Zeng, J. Yang, H. Yang, Y. Yang, and J. Zhao, "Bridging microstructure and sodium-ion storage mechanism in hard carbon for sodium ion batteries," *ACS Energy Letters*, vol. 9, no. 3, pp. 1184–1191, 2024. DOI: 10.1021/acsenergylett.3c02751.

[33] Q. Wang, X. Zhu, Y. Liu, Y. Fang, X. Zhou, and J. Bao, "Rice husk-derived hard carbons as high-performance anode materials for sodium-ion batteries," *Carbon*, vol. 127, pp. 658–666, 2018, ISSN: 0008-6223. DOI: https://doi.org/10.1016/j.carbon.2017.11.054.

[34] G. Hasegawa, K. Kanamori, N. Kannari, J.-i. Ozaki, K. Nakanishi, and T. Abe, "Hard carbon anodes for na-ion batteries: Toward a practical use," *ChemElectroChem*, vol. 2, no. 12, pp. 1917–1920, 2015. DOI: https://doi.org/10.1002/celc.201500412.

[35] Y. Zheng, Y. Lu, X. Qi, *et al.*, "Superior electrochemical performance of sodium-ion full-cell using poplar wood derived hard carbon anode," *Energy Storage Materials*, vol. 18, pp. 269–279, 2019, ISSN: 2405-8297. DOI: https://doi.org/10.1016/j.ensm.2018.09.002.

[36] S. T. Jackson and R. G. Nuzzo, "Determining hybridization differences for amorphous carbon from the xps c 1s envelope," *Applied Surface Science*, vol. 90, no. 2, pp. 195–203, 1995, ISSN: 0169-4332. DOI: https://doi.org/10.1016/0169-4332(95)00079-8.

[37] F. L. Coffman, R. Cao, P. A. Pianetta, S. Kapoor, M. Kelly, and L. J. Terminello, "Near-edge x-ray absorption of carbon materials for determining bond hybridization in mixed sp2/sp3 bonded materials," *Applied Physics Letters*, vol. 69, no. 4, pp. 568–570, 1996, ISSN: 0003-6951. DOI: 10.1063/1.117789.

[38] D. B. Schüpfer, F. Badaczewski, J. Peilstöcker, *et al.*, "Monitoring the thermally induced transition from sp3-hybridized into sp2-hybridized carbons," *Carbon*, vol. 172, pp. 214–227, 2021, ISSN: 0008-6223. DOI: https://doi.org/10.1016/j.carbon.2020.09.063.

[39] R. J. Gillespie and B. Silvi, "The octet rule and hypervalence: Two misunderstood concepts," *Coordination Chemistry Reviews*, vol. 233-234, pp. 53–62, 2002, ISSN: 0010-8545. DOI: https://doi.org/10.1016/S0010-8545(02)00102-9.

[40] J. Xiao, Q. Zhong, F. Li, J. Huang, Y. Zhang, and B. Wang, "Modeling the change of green coke to calcined coke using qingdao high-sulfur petroleum coke," *Energy & Fuels*, vol. 29, no. 5, pp. 3345–3352, 2015. DOI: 10.1021/acs.energyfuels.5b00021.

[41] L. L. Ban, D. Crawford, and H. Marsh, "Lattice-resolution electron microscopy in structural studies of non-graphitizing carbons from polyvinylidene chloride (pvdc)," *Journal of Applied Crystallography*, vol. 8, no. 4, pp. 415–420, 1975. DOI: https://doi.org/10.1107/S0021889875010904.

[42] Y. Yuan, Z. Chen, H. Yu, *et al.*, "Heteroatom-doped carbon-based materials for lithium and sodium ion batteries," *Energy Storage Materials*, vol. 32, pp. 65–90, 2020, ISSN: 2405-8297. DOI: https://doi.org/10.1016/j.ensm.2020.07.027.

[43] F. Wu, L. Liu, Y. Yuan, *et al.*, "Expanding interlayer spacing of hard carbon by natural k+ doping to boost na-ion storage," *ACS Applied Materials & Interfaces*, vol. 10, no. 32, pp. 27 030–27 038, 2018, ISSN: 1944-8244. DOI: 10.1021/acsami.8b08380.

[44] R. E. Franklin and J. T. Randall, "Crystallite growth in graphitizing and non-graphitizing carbons," *Proceedings of the Royal Society of London. Series A. Mathematical and Physical Sciences*, vol. 209, no. 1097, pp. 196–218, 1951. DOI: 10.1098/rspa.1951.0197.

[45] X. Dou, I. Hasa, D. Saurel, *et al.*, "Hard carbons for sodium-ion batteries: Structure, analysis, sustainability, and electrochemistry," *Materials Today*, vol. 23, pp. 87–104, 2019, ISSN: 1369-7021. DOI: https://doi.org/10.1016/j.mattod.2018.12.040.

[46] C. Yan, R. Xu, Y. Xiao, *et al.*, "Toward critical electrode/electrolyte interfaces in rechargeable batteries," *Advanced Functional Materials*, vol. 30, no. 23, p. 1 909 887, 2020. DOI: https://doi.org/10.1002/adfm.201909887.

[47] M. Gauthier, T. J. Carney, A. Grimaud, *et al.*, "Electrode–electrolyte interface in li-ion batteries: Current understanding and new insights," *The Journal of Physical Chemistry Letters*, vol. 6, no. 22, pp. 4653–4672, 2015. DOI: 10.1021/acs.jpclett.5b01727.

[48] M. Ricci, P. Spijker, F. Stellacci, J.-F. Molinari, and K. Voïtchovsky, "Direct visualization of single ions in the stern layer of calcite," *Langmuir*, vol. 29, no. 7, pp. 2207–2216, 2013, ISSN: 0743-7463. DOI: 10.1021/la3044736.

[49] P. C. Stern, "New environmental theories: Toward a coherent theory of environmentally significant behavior," *Journal of Social Issues*, vol. 56, no. 3, pp. 407–424, 2000. DOI: https://doi.org/10.1111/0022-4537.00175.

[50] X. Yu and A. Manthiram, "Electrode–electrolyte interfaces in lithium-based batteries," *Energy Environ. Sci.*, vol. 11, pp. 527–543, 3 2018. DOI: 10.1039/C7EE02555F.

[51] J. Song, B. Xiao, Y. Lin, K. Xu, and X. Li, "Interphases in sodium-ion batteries," *Advanced Energy Materials*, vol. 8, no. 17, p. 1 703 082, 2018. DOI: https://doi.org/10.1002/aenm.201703082.

[52] C. Bommier and X. Ji, "Electrolytes, sei formation, and binders: A review of nonelectrode factors for sodium-ion battery anodes," *Small*, vol. 14, no. 16, p. 1 703 576, 2018. DOI: https://doi.org/10.1002/smll.201703576.

[53] J. Fondard, E. Irisarri, C. Courrèges, M. R. Palacin, A. Ponrouch, and R. Dedryvère, "Sei composition on hard carbon in na-ion batteries after long cycling: Influence of salts (napf6, natfsi) and additives (fec, dmcf)," *Journal of The Electrochemical Society*, vol. 167, no. 7, p. 070 526, 2020. DOI: 10.1149/1945-7111/ab75fd.

[54] A. Laheäär, A. Jänes, and E. Lust, "Naclo4 and napf6 as potential non-aqueous electrolyte salts for electrical double layer capacitor application," *Electrochimica Acta*, vol. 82, pp. 309–313, 2012, ELECTROCHEMICAL FRONTIERS IN GLOBAL ENVIRONMENT AND ENERGY, ISSN: 0013-4686. DOI: https://doi.org/10.1016/j.electacta.2012.04.149.

[55] M. Winter, P. Novák, and A. Monnier, "Graphites for lithium-ion cells: The correlation of the first-cycle charge loss with the brunauer-emmett-teller surface area," *Journal of The Electrochemical Society*, vol. 145, no. 2, p. 428, 1998. DOI: 10.1149/1.1838281.

[56] F. Béguin, F. Chevallier, C. Vix-Guterl, *et al.*, "Correlation of the irreversible lithium capacity with the active surface area of modified carbons," *Carbon*, vol. 43, no. 10, pp. 2160–2167, 2005, ISSN: 0008-6223. DOI: https://doi.org/10.1016/j.carbon.2005.03.041.

[57] C. Bommier, W. Luo, W.-Y. Gao, A. Greaney, S. Ma, and X. Ji, "Predicting capacity of hard carbon anodes in sodium-ion batteries using porosity measurements," *Carbon*, vol. 76, pp. 165–174, 2014, ISSN: 0008-6223. DOI: https://doi.org/10.1016/j.carbon.2014.04.064.

[58] W. Luo, C. Bommier, Z. Jian, *et al.*, "Low-surface-area hard carbon anode for na-ion batteries via graphene oxide as a dehydration agent," *ACS Applied Materials & Interfaces*, vol. 7, no. 4, pp. 2626–2631, 2015. DOI: 10.1021/am507679x.

[59] N. Weadock, N. Varongchayakul, J. Wan, S. Lee, J. Seog, and L. Hu, "Determination of mechanical properties of the sei in sodium ion batteries via colloidal probe microscopy," *Nano Energy*, vol. 2, no. 5, pp. 713–719, 2013, ISSN: 2211-2855. DOI: https://doi.org/10.1016/j.nanoen.2013.08.005.

[60] X. Zhao, Y. Chen, H. Sun, *et al.*, "Impact of surface structure on sei for carbon materials in alkali ion batteries: A review," *Batteries*, vol. 9, no. 4, 2023. DOI: 10.3390/batteries9040226.

[61] A. Gomez-Martin, J. Martinez-Fernandez, M. Ruttert, M. Winter, T. Placke, and J. Ramirez-Rico, "Correlation of structure and performance of hard carbons as anodes for sodium ion batteries," *Chemistry of Materials*, vol. 31, no. 18, pp. 7288–7299, 2019, ISSN: 0897-4756. DOI: 10.1021/acs.chemmater.9b01768.

[62] E. Peled and S. Menkin, "Review—sei: Past, present and future," *Journal of The Electrochemical Society*, vol. 164, no. 7, A1703, 2017. DOI: 10.1149/2.1441707jes.

[63] "Carbon surface functionalities and sei formation during li intercalation," *Carbon*, vol. 92, pp. 193–244, 2015, ISSN: 0008-6223. DOI: https://doi.org/10.1016/j.carbon.2015.04.007.

[64] M. Montes-Morán, D. Suárez, J. Menéndez, and E. Fuente, "On the nature of basic sites on carbon surfaces: An overview," *Carbon*, vol. 42, no. 7, pp. 1219–1225, 2004, Carbon '03 Conference, ISSN: 0008-6223. DOI: https://doi.org/10.1016/j.carbon.2004.01.023.

[65] X. Zhao, Y. Ding, Q. Xu, X. Yu, Y. Liu, and H. Shen, "Low-temperature growth of hard carbon with graphite crystal for sodium-ion storage with high initial coulombic efficiency: A general method," *Advanced Energy Materials*, vol. 9, no. 10, p. 1 803 648, 2019. DOI: https://doi.org/10.1002/aenm.201803648.

[66] A. Oberlin and G. Terriere, "Graphitization studies of anthracites by high resolution electron microscopy," *Carbon*, vol. 13, no. 5, pp. 367–376, 1975, ISSN: 0008-6223. DOI: https://doi.org/10.1016/0008-6223(75)90004-4.

[67] P. J. F. Harris, "New perspectives on the structure of graphitic carbons," *Critical Reviews in Solid State and Materials Sciences*, vol. 30, no. 4, pp. 235–253, 2005. DOI: 10.1080/10408430500406265.

[68] R. Zaldivar and G. Rellick, "Some observations on stress graphitization in carbon-carbon composites," *Carbon*, vol. 29, no. 8, pp. 1155–1163, 1991, ISSN: 0008-6223. DOI: https://doi.org/10.1016/0008-6223(91)90033-F.

[69] Y. Marcus, "Ionic radii in aqueous solutions," *Chemical Reviews*, vol. 88, no. 8, pp. 1475–1498, 1988, ISSN: 0009-2665. DOI: 10.1021/cr00090a003.

[70] J. Mähler and I. Persson, "A study of the hydration of the alkali metal ions in aqueous solution," *Inorganic Chemistry*, vol. 51, no. 1, pp. 425–438, 2012, ISSN: 0020-1669. DOI: 10.1021/ic2018693.

[71] A. Cuesta, P. Dhamelincourt, J. Laureyns, A. Martínez-Alonso, and J. M. D. Tascón, "Comparative performance of x-ray diffraction and raman microprobe techniques for the study of carbon materials," *J. Mater. Chem.*, vol. 8, pp. 2875–2879, 12 1998. DOI: 10.1039/A805841E.

[72] H. Takagi, K. Maruyama, N. Yoshizawa, Y. Yamada, and Y. Sato, "Xrd analysis of carbon stacking structure in coal during heat treatment," *Fuel*, vol. 83, no. 17, pp. 2427–2433, 2004, ISSN: 0016-2361. DOI: https://doi.org/10.1016/j.fuel.2004.06.019.

[73] Y. Liu, B. V. Merinov, and W. A. Goddard, "Origin of low sodium capacity in graphite and generally weak substrate binding of na and mg among alkali and alkaline earth metals," *Proceedings of the National Academy of Sciences*, vol. 113, no. 14, pp. 3735–3739, 2016.

[74] L.-F. Zhao, Z. Hu, W.-H. Lai, *et al.*, "Hard carbon anodes: Fundamental understanding and commercial perspectives for na-ion batteries beyond li-ion and k-ion counterparts," *Advanced Energy Materials*, vol. 11, no. 1, p. 2 002 704, 2021. DOI: https://doi.org/10.1002/aenm.202002704.

[75] B. Xiao, T. Rojo, and X. Li, "Hard carbon as sodium-ion battery anodes: Progress and challenges," *ChemSusChem*, vol. 12, no. 1, pp. 133–144, 2019. DOI: https://doi.org/10.1002/cssc.201801879.

[76] C. Lastoskie, K. E. Gubbins, and N. Quirke, "Pore size heterogeneity and the carbon slit pore: A density functional theory model," *Langmuir*, vol. 9, no. 10, pp. 2693–2702, 1993, ISSN: 0743-7463. DOI: 10.1021/la00034a032.

[77] J. Jagiello and J. P. Olivier, "A simple two-dimensional nldft model of gas adsorption in finite carbon pores. application to pore structure analysis," *The Journal of Physical Chemistry C*, vol. 113, no. 45, pp. 19 382–19 385, 2009, ISSN: 1932-7447. DOI: 10.1021/jp9082147.

[78] C. L. Spiro, "Space-filling models for coal: A molecular description of coal plasticity," *Fuel*, vol. 60, no. 12, pp. 1121–1126, 1981, ISSN: 0016-2361. DOI: https://doi.org/10.1016/0016-2361(81)90064-8.

[79] S. Brunauer, P. H. Emmett, and E. Teller, "Adsorption of gases in multimolecular layers," *Journal of the American Chemical Society*, vol. 60, no. 2, pp. 309–319, 1938, ISSN: 0002-7863. DOI: 10.1021/ja01269a023.

[80] K. Sing, "The use of nitrogen adsorption for the characterisation of porous materials," *Colloids and Surfaces A: Physicochemical and Engineering Aspects*, vol. 187-188, pp. 3–9, 2001, ISSN: 0927-7757. DOI: https://doi.org/10.1016/S0927-7757(01)00612-4.

[81] J. L. C. Rowsell and O. M. Yaghi, "Effects of functionalization, catenation, and variation of the metal oxide and organic linking units on the low-pressure hydrogen adsorption properties of metal organic frameworks," *Journal of the American Chemical Society*, vol. 128, no. 4, pp. 1304–1315, 2006, ISSN: 0002-7863. DOI: 10.1021/ja056639q.

[82] L. D. Gelb and K. E. Gubbins, "Characterization of porous glasses: simulation models, adsorption isotherms, and the brunauer emmett teller analysis method," *Langmuir*, vol. 14, no. 8, pp. 2097–2111, 1998, ISSN: 0743-7463. DOI: 10.1021/la9710379.

[83] N. Elgrishi, K. J. Rountree, B. D. McCarthy, E. S. Rountree, T. T. Eisenhart, and J. L. Dempsey, "A practical beginner's guide to cyclic voltammetry," *Journal of Chemical Education*, vol. 95, no. 2, pp. 197–206, 2018, ISSN: 0021-9584. DOI: 10.1021/acs.jchemed.7b00361.

[84] A. Fick, "V. on liquid diffusion," *The London, Edinburgh, and Dublin Philosophical Magazine and Journal of Science*, vol. 10, no. 63, pp. 30–39, 1855. DOI: 10.1080/14786445508641925.

[85] S. W. Webb and K. Pruess, "The use of fick's law for modeling trace gas diffusion in porous media," *Transport in Porous Media*, vol. 51, no. 3, pp. 327–341, 2003, ISSN: 1573-1634. DOI: 10.1023/A:1022379016613.

[86] "Single electron transfer at an electrode," in *Elements of Molecular and Biomolecular Electrochemistry*. John Wiley & Sons, Ltd, 2006, ch. 1, pp. 1–77, ISBN: 9780471758075. DOI: https://doi.org/10.1002/0471758078.ch1.

[87] "Electron transfer, bond breaking, and bond formation," in *Elements of Molecular and Biomolecular Electrochemistry*. John Wiley & Sons, Ltd, 2006, ch. 3, pp. 182–250, ISBN: 9780471758075. DOI: https://doi.org/10.1002/0471758078.ch3.

[88] A. Lasia, "Electrochemical impedance spectroscopy and its applications," in *Modern Aspects of Electrochemistry*, B. E. Conway, J. O. Bockris, and R. E. White, Eds. Boston, MA: Springer US, 2002, pp. 143–248. DOI: 10.1007/0-306-46916-2_2.

[89] S. Wang, J. Zhang, O. Gharbi, V. Vivier, M. Gao, and M. E. Orazem, "Electrochemical impedance spectroscopy," *Nature Reviews Methods Primers*, vol. 1, no. 1, p. 41, 2021, ISSN: 2662-8449. DOI: 10.1038/s43586-021-00039-w.

[90] B.-Y. Chang and S.-M. Park, "Electrochemical impedance spectroscopy," *Annual Review of Analytical Chemistry*, vol. 3, no. Volume 3, 2010, pp. 207–229, 2010, ISSN: 1936-1335. DOI: https://doi.org/10.1146/annurev.anchem.012809.102211.

[91] B.-A. Mei, O. Munteshari, J. Lau, B. Dunn, and L. Pilon, "Physical interpretations of nyquist plots for edlc electrodes and devices," *The Journal of Physical Chemistry C*, vol. 122, no. 1, pp. 194–206, 2018, ISSN: 1932-7447. DOI: 10.1021/acs.jpcc.7b10582.

[92] M. Naderi, "Chapter fourteen - surface area: Brunauer–emmett–teller (bet)," in *Progress in Filtration and Separation*, S. Tarleton, Ed., Oxford: Academic Press, 2015, pp. 585–608, ISBN: 978-0-12-384746-1. DOI: https://doi.org/10.1016/B978-0-12-384746-1.00014-8.

[93] B.-J. Kim, Y.-S. Lee, and S.-J. Park, "A study on pore-opening behaviors of graphite nanofibers by a chemical activation process," *Journal of Colloid and Interface Science*, vol. 306, no. 2, pp. 454–458, 2007, ISSN: 0021-9797. DOI: https://doi.org/10.1016/j.jcis.2006.10.038.

[94] K.-l. Hong, L. Qie, R. Zeng, *et al.*, "Biomass derived hard carbon used as a high performance anode material for sodium ion batteries," *J. Mater. Chem. A*, vol. 2, pp. 12 733–12 738, 32 2014. DOI: 10.1039/C4TA02068E.

[95] Z. Li, C. Lu, Z. Xia, Y. Zhou, and Z. Luo, "X-ray diffraction patterns of graphite and turbostratic carbon," *Carbon*, vol. 45, no. 8, pp. 1686–1695, 2007, ISSN: 0008-6223. DOI: https://doi.org/10.1016/j.carbon.2007.03.038.

[96] S.-J. Park and J.-S. Kim, "Modifications produced by electrochemical treatments on carbon blacks: Microstructures and mechanical interfacial properties," *Carbon*, vol. 39, no. 13, pp. 2011–2016, 2001, ISSN: 0008-6223. DOI: https://doi.org/10.1016/S0008-6223(01)00015-X.

[97] B. E. Warren, "X-Ray Diffraction Study of Carbon Black," *The Journal of Chemical Physics*, vol. 2, no. 9, pp. 551–555, 1934, ISSN: 0021-9606. DOI: 10.1063/1.1749528.

[98] A. K. Kercher and D. C. Nagle, "Microstructural evolution during charcoal carbonization by x-ray diffraction analysis," *Carbon*, vol. 41, no. 1, pp. 15–27, 2003, ISSN: 0008-6223. DOI: https://doi.org/10.1016/S0008-6223(02)00261-0.

[99] F. Fina, S. K. Callear, G. M. Carins, and J. T. S. Irvine, "Structural investigation of graphitic carbon nitride via xrd and neutron diffraction," *Chemistry of Materials*, vol. 27, no. 7, pp. 2612–2618, 2015, ISSN: 0897-4756. DOI: 10.1021/acs.chemmater.5b00411.

[100] S. Komaba, W. Murata, T. Ishikawa, *et al.*, "Electrochemical na insertion and solid electrolyte interphase for hard-carbon electrodes and application to na-ion batteries," *Advanced Functional Materials*, vol. 21, no. 20, pp. 3859–3867, 2011. DOI: https://doi.org/10.1002/adfm.201100854.

[101] H. Alptekin, H. Au, A. C. Jensen, *et al.*, "Sodium storage mechanism investigations through structural changes in hard carbons," *ACS Applied Energy Materials*, vol. 3, no. 10, pp. 9918–9927, 2020. DOI: 10.1021/acsaem.0c01614.

[102] M. Thompson, Q. Xia, Z. Hu, and X. Zhao, "A review on biomass-derived hard carbon materials for sodium-ion batteries," *Materials Advances*, vol. 2, 2021. DOI: 10.1039/D1MA00315A.

[103] N. Schulz, R. Hausbrand, C. Wittich, L. Dimesso, and W. Jaegermann, "Xps-surface analysis of sei layers on li-ion cathodes: Part ii. sei-composition and formation inside composite electrodes," *Journal of The Electrochemical Society*, vol. 165, no. 5, A833, 2018. DOI: 10.1149/2.0881803jes.

[104] R. Mogensen, D. Brandell, and R. Younesi, "Solubility of the solid electrolyte interphase (sei) in sodium ion batteries," *ACS Energy Letters*, vol. 1, no. 6, pp. 1173–1178, 2016. DOI: 10.1021/acsenergylett.6b00491.

[105] C. Bommier and X. Ji, "Electrolytes, sei formation, and binders: A review of nonelectrode factors for sodium-ion battery anodes," *Small*, vol. 14, no. 16, p. 1 703 576, 2018. DOI: https://doi.org/10.1002/smll.201703576.

[106] C. Zhang, D. He, J. Ma, W. Tang, and T. D. Waite, "Faradaic reactions in capacitive deionization (cdi) - problems and possibilities: A review," *Water Research*, vol. 128, pp. 314–330, 2018, ISSN: 0043-1354. DOI: https://doi.org/10.1016/j.watres.2017.10.024.

[107] E. Frackowiak and F. Béguin, "Carbon materials for the electrochemical storage of energy in capacitors," *Carbon*, vol. 39, no. 6, pp. 937–950, 2001, ISSN: 0008-6223. DOI: https://doi.org/10.1016/S0008-6223(00)00183-4.